THE JOURNAL OF PHYSICAL CHEMISTRY B
A JOURNAL OF THE AMERICAN CHEMICAL SOCIETY

pubs.acs.org/JPCB
Article

Pyrrolidinium and Imidazolium-Based Ionic Liquids as Electrolytes for $Na_{0.67}Ni_{0.33}Mn_{0.67}O_2$ Positive Electrode for Sodium−Ion Batteries

Leandro S. Domingues, Roberto M. Torresi, Vincent Vivier, Mireille Turmine,* Vitor L. Martins,* and Hercilio G. de Melo*

Cite This: https://doi.org/10.1021/acs.jpcb.5c07871

ABSTRACT: In this paper, the electrochemical performance of two nitrogen-based ionic liquids (ILs), 1-butyl-1-methylpyrrolidinium bis(trifluoromethylsulfonyl)imide (BMPyr-TFSI) and 2,3-dimethylimidazolium bis(trifluoromethylsulfonyl)imide (BMMI-TFSI), with different concentrations of NaTFSI, as electrolytes for the $Na_{0.67}Ni_{0.33}Mn_{0.67}O_2$ (NNM) positive electrode for sodium−ion batteries (SIBs) were compared with the conventional 1.0 mol L^{-1} $NaClO_4$ in carbonate electrolyte. Moreover, the influence of salt concentration on the physicochemical properties of both ILs was evaluated. Amidst the neat ILs, BMPyr-TFSI showed better transport properties than BMMI-TFSI, whereas, for NaTFSI-mixtures, adding salt was detrimental to the ILs' properties. The poorer transport properties of the ILs compared to those of the carbonate electrolyte negatively impact the NNM electrode performance. At C/10, the highest discharge capacity obtained in IL mixtures was 40 mA h g^{-1} for BMPyr-TFSI with 0.5 mol L^{-1} of NaTFSI, compared to 59 mA h g^{-1} for NNM in $NaClO_4$ electrolyte. Lowering the current density improved the performance of NNM in both BMPyr and BMMI-based mixtures, achieving specific capacities and Coulombic efficiencies above 53 mA h g^{-1} and 96%, respectively, at C/50. This approach has proven effective in overcoming the kinetic limitations due to the poorer transport properties displayed by ILs, encouraging the implementation of these electrolytes in SIBs.

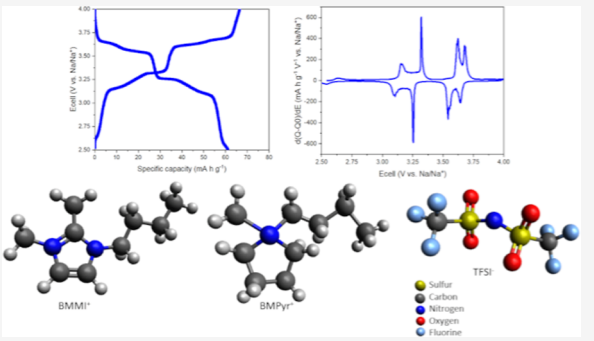

INTRODUCTION

The environmental impact of producing energy from the combustion of fossil fuels has encouraged research into renewable energy sources and, at the same time, increased the demand for appropriate energy storage systems.[1] Secondary batteries have emerged as an interesting prospect, with lithium-ion batteries (LIBs) being the most prominent. However, the concentration of Li reserves in a few countries and their ongoing extraction have reduced its availability, which could lead to increased costs and supply shortages.[2−4] Moreover, current extraction methods pose some environmental risks.[5] As a result, replacing Li with other materials that have similar properties is becoming a critical issue. One promising approach is the use of sodium−ion batteries (SIBs), leveraging sodium's abundance and its chemical similarity to lithium.[3,6]

Over the years, various materials have been studied for use as positive electrodes in SIBs, in which layered oxide systems are the most widespread due to their structural flexibility and versatility.[7,8] Their intrinsic structure allows better diffusion of sodium ions, thereby enhancing rate capability.[7−9] One potential layered oxide material commonly studied for use as the positive electrode in SIBs is $Na_{0.67}Ni_{0.33}Mn_{0.67}O_2$ (NNM). Depending on the oxygen stacking ordering, this compound can exhibit two different structures: prismatic (P) and octahedral (O)-type.[7] Although octahedral-type cathodes typically exhibit a higher Na storage capacity compared to prismatic systems, they are reported to suffer from poor rate capability and inferior cycling stability.[10] Conversely, the crystalline arrangement of the prismatic structure enables faster Na^+ diffusion due to the presence of open pathways.[11] Moreover, the P2-type compound (2 stands for the number of repeated oxygen layers within the unit cell) has a specific theoretical capacity of 173 mA h g^{-1} (assuming the transfer of 2/3 mol of Na^+), which is comparable to some layered oxides used in lithium-ion systems.[12,13] However, studies on this material in the literature primarily focus on changes in electrode composition, rather than on suitable electrolytes.[14−19] These latter play a critical role in the battery performance since they facilitate ionic conduction between the electrodes in a cell.

Received: November 18, 2025
Revised: January 4, 2026
Accepted: January 5, 2026

In addition to high ionic conductivity, the electrolyte must display good thermal, chemical, and electrochemical stability, low reactivity and low corrosivity toward other cell components, and be environmentally friendly.[20,21] In metal-ion systems, organic electrolytes are typically used as solvents. Nonetheless, due to fire hazard associated with their volatility,[22] research into new electrolytes with properties similar to those of conventional systems is becoming important for SIBs. In this context, electrolytes based on ionic liquids (ILs) are excellent candidates. Their negligible flammability practically eliminates the risk of fire in batteries,[23] promoting adequate safety levels for SIB operation. Moreover, this family of electrolytes can achieve conductivity comparable to conventional systems, along with exceptional chemical and electrochemical stability.[24−26]

Risthaus et al. published in 2018 one of the few articles on the implementation of ILs as substitutes for conventional organic systems for NNM.[27] The authors evaluated the performance of the positive electrode in the presence of 1-butyl-1-methylpyrrolidinium bis(trifluoromethylsulfonyl)imide containing 1.0 mol L^{-1} NaTFSI, using galvanostatic charge/discharge cycles at 60 °C, scanning electron microscopy (SEM), X-ray diffraction (XRD), and X-ray absorption spectroscopy (sXAS). At 60 °C, the electrochemical results demonstrated enhanced electrode performance in the nitrogen-based electrolyte, achieving a higher specific capacity than experiments performed at room temperature using the conventional 1.0 mol L^{-1} $NaPF_6$ in ethylene carbonate (EC)/dimethyl carbonate (DMC) (EC/DMC 1:1 v/v) electrolyte.

Despite the promising results obtained by Risthaus et al.,[27] it is acknowledged that the performance of ILs in energy storage devices is also significantly influenced by the transport properties of the electrolyte.[28] The selection of the optimum cation−anion combination,[29] in conjunction with the concentration of salt in the electrolyte,[3,30] play a fundamental role, as they affect ionic transport and energy supply rate. Thus, for better comprehension of the applicability of this family of electrolytes for NNM electrode material, it is essential to evaluate how these properties influence the battery's performance.

The present work aims to evaluate the feasibility of two nitrogen-based ILs families, namely, 1-butyl-1-methylpyrrolidinium bis(trifluoromethylsulfonyl)imide (BMPyr-TFSI) and 1-butyl-2,3-dimethylimidazolium bis(trifluoromethylsulfonyl)-imide (BMMI-TFSI), and their mixtures with different NaTFSI salt concentrations as electrolytes for NNM. The motivation for evaluating these two electrolyte families lies in their distinct properties. Imidazolium salts exhibit high chemical and electrochemical stability owing to the configuration of the central ring.[31,32] In contrast, pyrrolidinium shows good transport properties attributable to its quasi-flat geometry, which hinders steric effects that are detrimental to ionic mobility.[33,34] The investigation was performed using electrochemical techniques, specifically electrochemical impedance spectroscopy (EIS), to access information related to the electrode properties, and charging−discharging experiments at various C-rates to evaluate NNM performance in the different electrolytes. In order to provide a comprehensive assessment of the electrochemical tests, the physicochemical properties, density, viscosity, and conductivity for the different ILs were determined. In addition, the diffusion coefficient of Na^+ in these ILs was estimated. As an additional analysis, the thermal properties of the selected ILs were analyzed.

METHODS

Ionic Liquids

1-butyl-1-methylpyrrolidinium bis(trifluoromethylsulfonyl)imide (BMPyr-TFSI) and 1-butyl-2,3-dimethylimidazolium bis-(trifluoromethylsulfonyl)imide (BMMI-TFSI) were selected as the nitrogen-based ILs. The former was commercially provided by Iolitec (99.9% purity), while the latter was synthesized according to previous reports.[25,35] Sodium bis(trifluoromethylsulfonyl)imide (NaTFSI), Sigma-Aldrich (99.5% purity), was selected as the salt.

The different mixtures were prepared in an argon-filled glovebox (oxygen and water contents below 1.0 ppm) at varying salt concentrations: 0.5 and 1.0 mol L^{-1} for BMPyr-TFSI, and 0.5 and 0.83 mol L^{-1} for BMMI-TFSI. The maximum concentration of 0.83 mol L^{-1} for BMMI-TFSI corresponds to the solubility of this salt. Prior to the assembly of the batteries, the ILs were dried at 100 °C for 24 h on a hot plate within the glovebox. The water content of the electrolytes was measured using a Karl Fischer coulometric titrator (Metrohm) to ensure a maximum water content of less than 10 ppm.

Physicochemical Properties

The physicochemical properties of the ILs were determined over a temperature range from 25 to 80 °C. Density and viscosity measurements were performed using a digital densimeter/viscometer (SVM 3000/G2, Anton Paar) with a thermoregulator. Ionic conductivity was measured by EIS, using an Autolab potentiostat (PGSTAT204, Metrohm) equipped with a Microcell HC 70 cell stand with a temperature controller (Peltier effect). The EIS spectra were obtained over a frequency range from 100 kHz to 10 mHz, with a perturbation amplitude of 10 mV and with six points acquired per decade. The cell constant was obtained using an aqueous solution of 0.01 mol L^{-1} KCl.

Thermal Analysis

In order to access information on possible phase transitions on the different ILs and their mixtures with NaTFSI, differential scanning calorimetry (DSC) analyses were carried out using a T.A. Instruments—DSC Q10, coupled with a refrigerated cooling system (RCS) under nitrogen atmosphere. It is important to highlight that the neat IL BMMI-TFSI was not included in the analysis because its glass transition temperature (T_g) is reported to be lower than the minimum temperature reached by the equipment (−80 °C).[25,36] Prior to analysis, the samples for DSC were weighed and hermetically sealed within an aluminum pan inside the glovebox to avoid air exposure. The measurements were performed by initially cooling the samples (at a rate of 20 °C min^{-1}) to −80 °C and maintaining them at this temperature for 2 min, and then heating at a rate of 20 °C min^{-1} up to 300 °C.

Active Material Synthesis

NNM was selected as the positive electrode of the battery. The active material was synthesized by solid-state chemistry using the following precursors: anhydrous sodium carbonate (Na_2CO_3), Syth (99.5% purity); nickel(II) acetate tetrahydrate ($C_4H_6NiO_4{\cdot}4H_2O$), and manganese(II) acetate tetrahydrate ($Mn(H_3CCOO)_2{\cdot}4H_2O$), Sigma-Aldrich (98% and 99% purity, respectively). The precursors were weighed separately to ensure a stoichiometric ratio of 0.8:0.6:0.4 between Na, Mn, and Ni. Sodium excess was added to compensate for losses during sintering.[37] The compounds were then mixed using an agate mortar and pestle, prior to being transferred into a muffle furnace (EGD3P-S) using a ceramic crucible. The sintering process was carried out in two stages. Initially, the powder was heated at 100 °C for 12 h to remove water, followed by a heat treatment up to 850 °C (at a rate of 2 °C min^{-1}) for 12 h, and then cooled to room temperature in air. The sintering temperature was selected based on the results reported by Liu et al.[37] A low heating rate was used to avoid the formation of NiO impurities in the active material.[18] The final crystal structure was characterized by XRD using a Shimadzu

https://doi.org/10.1021/acs.jpcb.5c07871
J. Phys. Chem. B XXXX, XXX, XXX−XXX

XRD7000 diffractometer equipped with a Cu Kα source generated at 40 kV and 30 mA. The XRD spectrum of NNM powder was performed in the 2θ range from 10° to 80° and is presented in the Supporting Information section (Figure S1).

Electrode Preparation and Battery Assembly

The positive electrode was prepared by mixing 90 wt % active material, 5 wt % polyvinylidene fluoride (PVDF) binder, and 5 wt % Super C_{65} conductive additive (500 mg of total solids). The slurry was prepared using the following procedure: the PVDF binder was dissolved in 1.5 mL of *N*-methyl-pyrrolidone (NMP) using an Eppendorf with eight ZrO_2 spheres of 1.5 mm; then, both Super C_{65} and NNM powder were added to the Eppendorf, and the assembly was mixed using a ball mill (Solab) for 3 h at a frequency of 617 bpm. The final slurry was then doctor-bladed onto an aluminum foil (resulting in a final wet film thickness of 200 μm) and dried at 80 °C under vacuum for 24 h. The electrodes were punched into discs with a diameter of 16 mm with an average load mass of 5.13 mg cm^{-2}. Prior to battery assembly, the electrode surface was characterized by SEM (FEG Inspect 50 scanning electron microscope). The SEM micrograph of the electrode and the energy dispersive spectroscopy (EDS) analysis are presented in the Supporting Information section (Figures S2 and S3, respectively).

CR2032 coin cells were assembled in an argon-filled glovebox, where the levels of water and oxygen were maintained below 1.0 ppm. The positive electrode consisted of NMM, while a 10 mm-diameter sodium disk served as the negative electrode. A 19 mm glass fiber (Whatman GF/F) was used as separator.

Electrochemical Characterization

Electrochemical measurements were carried out using the BioLogic BCS-805 battery cycler. To evaluate electrode performance under different conditions, the batteries were galvanostatically charged and discharged over a potential range of 2.5−4.0 V vs Na/Na$^+$ at varying C-rates (for the system under study, 1C is equivalent to 173 mA h g^{-1}). The higher cell potential limit was chosen on the basis that NNM undergoes an irreversible phase transition when 2/3 mol of Na$^+$ is removed from the crystal lattice, as previously reported.[38,39] As an additional tool, the potential profiles obtained were analyzed using the differential capacity curves (dQ/dE vs E) to determine the effect of the different media in the intercalation/deintercalation process of Na$^+$. The conventional electrolyte $NaClO_4$ (1.0 mol L^{-1}) in a 1:1 (v/v) mixture of EC and propylene carbonate (PC) was used for comparison. All the experiments were performed at room temperature (25 °C).

Sodium Diffusion Coefficient Determination

EIS measurements were conducted to estimate the sodium diffusion coefficient in the different IL-based mixtures and in the conventional perchlorate electrolyte. All experiments were performed at room temperature, using a Swagelok cell with a 10 mm sodium disk as the counter and reference electrodes, and an 8 mm copper disk serving as the working electrode. The approach adopted in this study was analogous to that used by previous researchers[40−43] prior to the acquisition of the EIS spectrum. The cells were initially subjected to a galvanostatic cathodic current density of 40 μA cm^{-2} to reach a stationary potential between sodium stripping from the counter electrode and its plating onto the copper electrode. After 1 h under these conditions, the system was left at the open circuit potential for an additional 1 h prior to the impedance measurement. The EIS spectra were obtained over a frequency range from 100 kHz to 10 mHz, with a perturbation amplitude of 10 mV and with six points acquired per frequency decade. The impedance data were fitted to determine the diffusion coefficient from the low-frequency region. The latter will be further discussed in the results and discussions section.

CEI Properties

To provide further insights into the cycling results across different electrolytes, EIS experiments were conducted to assess the properties of the electrode and the cathode solid electrolyte interphase (CEI). For this purpose, fresh batteries (half-cell system) were assembled and subjected to galvanostatic charge and discharge cycles over the potential range of 2.5−4.0 V vs Na/Na$^+$ with impedance spectra acquired before and after the cycles. For the conventional electrolyte, two cycles were carried out at C/20 (specific current of 8.65 mA g^{-1}), while for the IL*s* mixtures, two cycles at C/50 (3.46 mA g^{-1}) were carried out. All EIS diagrams were obtained using the same parameters described above.

RESULTS AND DISCUSSION

Physicochemical Properties

Density is a critical parameter in the design of lighter energy storage systems,[44] and its value is used to calculate the IL molar conductivity (Λ_m).[24] Figure 1 shows the density

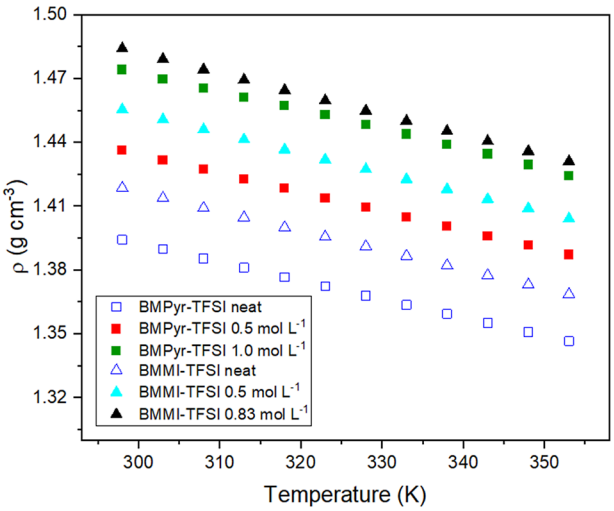

Figure 1. Density variation as a function of temperature for the different mixtures of nitrogen-based ILs.

variation with temperature for the different ILs and their mixtures, showing that it decreases linearly with increasing temperature. Among the various electrolytes, the imidazolium-based cation shows a higher density than the pyrrolidinium counterpart. As demonstrated in previous studies,[25,45] BMMI$^+$ is less geometrically packed than BMPyr$^+$ owing to the presence of a second methyl group on the imidazolium ring. This results in a larger volume (266 Å^3 against 253 Å^3). However, a more plausible explanation for the observed behavior is provided by the differences in molar mass between the two species: the molecular weight of BMMI$^+$ is 153.25 g mol^{-1}, while that of BMPyr$^+$ is 142.27 g mol^{-1}.

The addition of the sodium salt has been demonstrated to increase the IL density for all electrolytes. As shown in Table 1,

Table 1. Density, Viscosity, and Conductivity of the Nitrogen-Based ILs at 25 °C.

cation−anion pair	NaTFSI concentration (mol L^{-1})	density (g cm^{-3})	viscosity (mPa s)	conductivity (mS cm^{-1})
BMPyr-TFSI	--	1.394	79.3	2.64
	0.5	1.436	173.6	1.31
	1.0	1.474	357.5	0.58
BMMI-TFSI	--	1.418	99.9	1.96
	0.5	1.455	189.2	1.15
	0.83	1.491	301.8	0.83

https://doi.org/10.1021/acs.jpcb.5c07871
J. Phys. Chem. B XXXX, XXX, XXX−XXX

at 25 °C, the average increase for BMPyr-TFSI is 3.0% and 5.8% for 0.5 and 1.0 mol L^{-1} NaTFSI. In the case of BMMI-TFSI, the average increase is 2.6% and 5.1% for 0.5 and 0.83 mol L^{-1} NaTFSI, respectively. This outcome was anticipated, as the addition of alkali metal salts to ILs results in ion clustering, accompanied by changes in ion packing, thus contributing to an increase in overall density.[46,47]

Figure 2 displays the Arrhenius plots of the viscosity (η) (Figure 2a) and conductivity (σ) (Figure 2b) for the pure ILs

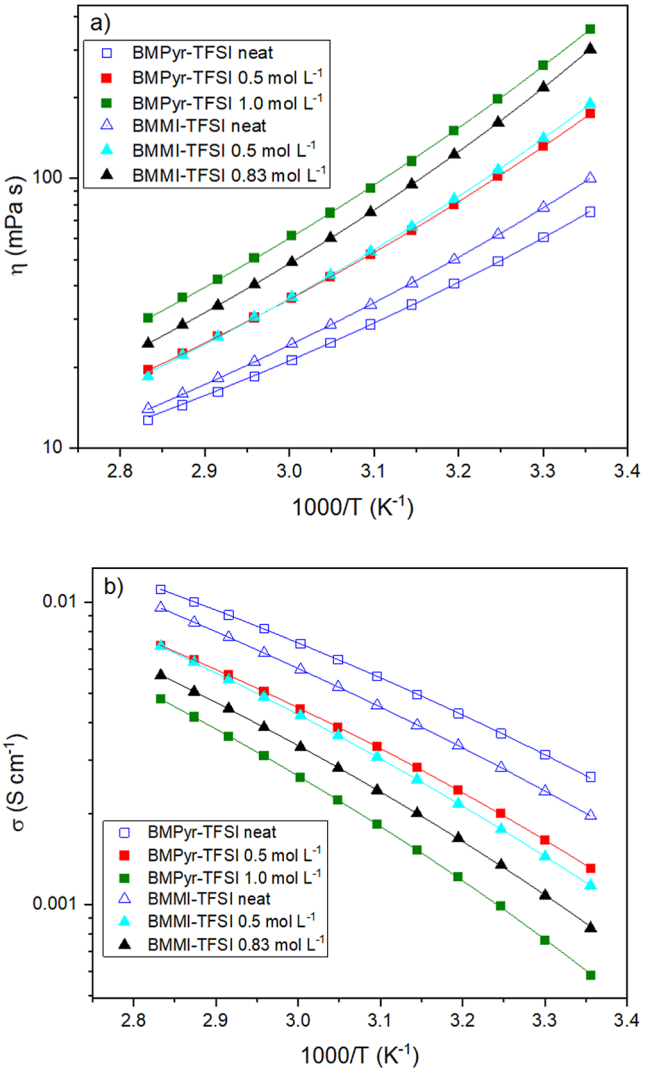

Figure 2. Arrhenius plots for the variation of viscosity and conductivity as a function of temperature for the different mixtures of nitrogen-based ILs (the symbols stand for the experimental data and the lines for the fitting with the VFT equations): (a) viscosity; (b) conductivity.

and their mixtures with NaTFSI, which were fitted using the Vogel–Fulcher–Tammann (VFT) eqs (eqs 1 and 2). VFT is based on the Arrhenius equation; however, it is regarded as a more suitable method for liquids undergoing a glass transition transformation;[48] it is, therefore, commonly used to analyze viscosity and conductivity data for ILs.[25,49−52] Moreover, it generally provides a better fit than the Arrhenius and Litovitz equations.[53−56]

$$\eta = \eta_0 \, e\left(\frac{D_{VFT} \times T_0}{T - T_0}\right) \quad (1)$$

$$\sigma = \sigma_0 \, e\left(\frac{-D_{VFT} \times T_0}{T - T_0}\right) \quad (2)$$

In eq 1 and 2, η_0 and σ_0 are the pre-exponential factors, T and T_0 are the absolute temperature and the "ideal glass transition temperature", respectively.[57] D_{VFT} corresponds to the fragility of the IL, and refers to changes in the property produced by temperature.[50,58] The high values obtained indicate that the properties show reduced susceptibility to temperature fluctuations, signifying a less fragile liquid state.[49] The parameters from the fitting procedure are presented in the Supporting Information section (Tables S1 and S2).

Viscosity and conductivity play major roles in the design of electrolytes for batteries, showing a reciprocal relationship: that is, an increase in viscosity corresponds to a decrease in conductivity. The former is associated with the liquid's flow resistance, while the latter includes the mobility of charge carriers. These two parameters can be influenced by the intrinsic characteristics of the IL cation and anion, such as their nature, size, structure, chemical functionalities, molecular weight, chain flexibility, and the presence of heteroatoms.[24,29,45,49,59−63] Accordingly, the selection of the cation and anion combination is a crucial factor, as it can either diminish or augment these interactions and, consequently, affect the transport properties of the IL.[63]

Concerning the neat ILs, BMMI-TFSI (blue triangle) showed a higher viscosity (Figure 2a) and a lower conductivity (Figure 2b) than the pyrrolidinium-based cation, BMPyr-TFSI (blue square). As previously reported by other authors, the inherent planarity of the $BMMI^+$ ring favors ion−ion interactions,[25] thereby increasing the flow resistance. Moreover, the best transport properties displayed by BMPyr-TFSI can be attributed to its quasi-flat geometry,[33] which mitigates steric effects that could impede ionic mobility.[34] An examination of the mixture of salts reveals a correlation between the increase in NaTFSI concentration and the concomitant increase in η and decrease in σ. As shown in Table 1, for $BMPyr^+$ electrolytes, at 25 °C, the viscosity increases 2.19 and 4.51 times when 0.5 and 1.0 mol L^{-1} of NaTFSI were added to the electrolytes. At the same time, conductivity decreases by 0.50 and 0.78 times from the initial value. For $BMMI^+$ electrolytes, the increase in η was 1.9 and 3.0 times with the addition of 0.5 and 0.83 mol L^{-1} of NaTFSI, whereas σ shows a decrease of 0.41 and 0.58 times the value obtained for the neat IL. This same trend was confirmed in other studies exploring the physicochemical properties of IL-based electrolytes with different salt concentrations.[3,30,36,50,64−68] For NaTFSI-based systems, the sodium ion tends to coordinate with three $TFSI^-$ anion, resulting in the formation of $[Na(TFSI)_3]^{2-}$, as demonstrated by Monti et al.[30] using Raman spectroscopy and DFT calculations. Since the charge density of Na^+ is higher compared to organic cations, Na-TFSI interactions are enhanced as the number of ionic species increases in the medium.[69−71] The formation of more $[Na(TFSI)_3]^{2-}$ aggregates impairs the transport properties.

An interesting methodology for examining the physicochemical characteristics of different IL families and collecting data on their ionicity is to correlate the molar conductivity, Λ_m,

https://doi.org/10.1021/acs.jpcb.5c07871
J. Phys. Chem. B XXXX, XXX, XXX−XXX

with the fluidity (η^{-1}), which is referred to as Walden's plot. The ionicity of an IL is particularly significant because it is directly associated with the availability of charge carriers.[72] To increase the ionicity, it is imperative that both the cation and the anion exhibit minimal coordination capacity. This, in turn, leads to an increase in the density of species that are responsible for the transport properties. The formation of ionic pairs can result in the creation of neutral aggregates, reducing the ionicity of the IL.[73]

Figure 3 shows a log−log representation of Walden's plot, while its linear representation is shown in the Supporting Information section (Figure S4). For a very dilute solution (dotted reference line in Figure 3), an ideal behavior is expected, corresponding to total ionization. All the tested liquids fall below this line, suggesting the existence of ionic associations resulting from aggregate formation.[73] Interestingly, when comparing the two neat nitrogen families, BMPyr-TFSI is closer to the ideal dotted line in Figure 3 than BMMI-TFSI. In their study, Ramirez et al.[45] used EIS to compare the ionic conductivity of BMMI-B(CN_4) and BMPyr-B(CN_4), focusing exclusively on the contribution of ionic species. They further used nuclear magnetic resonance (NMR) to estimate the contribution of all species to the overall conductivity. Through the calculation of the ratio between the two conductivities, it was ascertained that BMPyr has a higher ratio than BMMI, indicating that the former would have more species contributing to conductivity, thus suggesting that the imidazolium cation has a greater tendency to form neutral aggregates than $BMPyr^+$, which is in agreement with our results. In the presence of the Na^+ salt, the curves for BMPyr-based and BMMI-based electrolytes shifted, moving further away from the reference curve, a tendency that is accentuated with increasing salt concentration. This was an expected outcome, as increasing the concentrations of Na^+ and $TFSI^-$ in the medium must result in a notable increase in the frequency of interactions and the formation of aggregates, leading to a reduction in the electrolyte's ionicity.

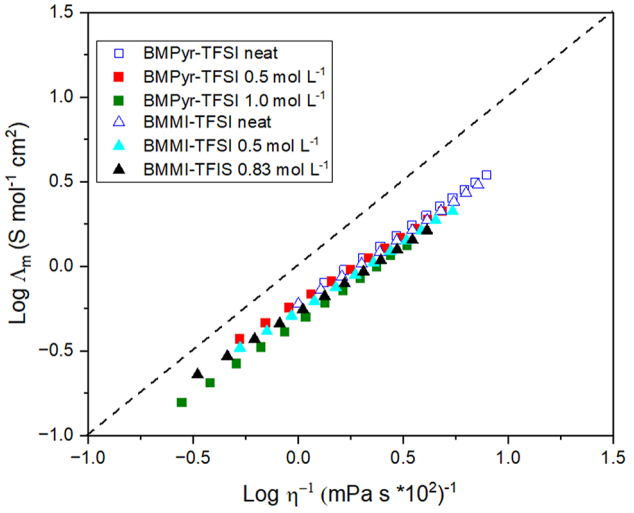

Figure 3. Log−log representation of Walden's plot for the different mixtures of nitrogen-based ILs.

Thermal Analysis

Figure 4 shows the results of the DSC investigation for the ILs and their mixtures with NaTFSI. Concerning the pyrrolidinium-based electrolytes, the DSC pattern for the neat IL (Figure 4a) reveals the existence of one exothermic peak, near −45 °C, and two endothermic peaks near −25 and −15 °C, which are in agreement with previous studies.[74,75] The exothermic peak is associated with a crystalline phase,[74,75] while the two endothermic peaks reflect the two stages of the melting of the IL.[75,76] Given the reported T_g of BMPyr-TFSI, which is estimated to range from −87[75] and −89[3] °C, it is not expected to be observed in the thermogram. Consequently, the results are not included in the study.

Adding NaTFSI changed the DSC profiles compared to the salt-free condition. For the lowest salt concentration (Figure 4b—red curve), no apparent peaks are observed, whereas for 1.0 mol L^{-1} (Figure 4c—green curve), two endothermic peaks, near −65 and 16 °C, are present. These changes can be ascribed to the disorder promoted by Na^+ in the pyrrolidinium-based IL.[3,77,78] As shown by Noor et al.,[3] from 0.3 mol L^{-1} of NaTFSI the IL's crystallization seems to be completely inhibited, and consequently, no endothermic peak associated with BMPyr-TFSI crystallization is expected to be observed. Moreover, the T_g tends to shift to higher temperatures as the salt concentration increases in the electrolyte, which can be associated with the formation of Na^+ complexes and clusters.[77] For instance, the T_g of a 0.5 mol L^{-1} of NaTFSI, is reported to be approximately −80 °C[3], which accounts for the absence of its respective endothermic peak in Figure 4b. Conversely, for BMPyr-TFSI with 1.0 mol L^{-1} of NaTFSI (Figure 4c), the first endothermic peak could be correlated to the electrolyte's T_g, while the second one could be associated with the distinct conformers of $TFSI^-$.[77]

For the BMMI-based mixtures (Figure 4d,e), a single endothermic peak is observed at each concentration. For 0.5 mol L^{-1} of NaTFSI (Figure 4d), the peak is situated at approximately −67 °C, while for 0.83 mol L^{-1} (Figure 4e), it is close to −63 °C. Both peaks can be associated with the electrolyte's glass transition,[30,36] similarly to what was previously reported for BMMI-TFSI mixtures containing LiTFSI salt.[36] Similarly to the response for the BMPyr-based electrolyte, T_g increases with the Na^+ concentration, indicating an increase in Na-ion interactions. When comparing the two families of ILs for the same salt concentration (0.5 mol L^{-1} of NaTFSI), a higher T_g temperature is observed for the imidazolium ion-based medium. This response suggests that the interactions generated by the sodium's presence have a more significant impact on the dynamics of this electrolyte, consistent with its physicochemical properties.

Electrochemical Characterization

Figure 5 shows the potential profiles for NNM (with a theoretical specific capacity of 173 mA h g^{-1}) at different C-rates for the various electrolytes. For better visualization, only Figure 5e shows the corresponding specific currents for each C-rate. The potential curves in the conventional electrolyte (Figure 5a) exhibit four plateaus. During the discharge, these plateaus are located at about 3.10, 3.25, 3.50, and 3.60 V vs Na/Na^+, whereas during charging, they are located at about 3.15, 3.30, 3.60, and 3.70 V vs Na/Na^+. These plateaus agree with those observed in other NNM studies[18,37,79,80] and are associated with redox reactions governed by $Ni^{2+}/Ni^{3+}/Ni^{4+}$ couples, as verified by X-ray photoelectron spectroscopy analyses.[39,81,82] XRD analyses performed by Lu et al.,[83] Wen et al.,[84] and Wang et al.[85] show that NNM does not undergo phase transition in the potential range between 2.0 and 4.0 V

https://doi.org/10.1021/acs.jpcb.5c07871
J. Phys. Chem. B XXXX, XXX, XXX−XXX

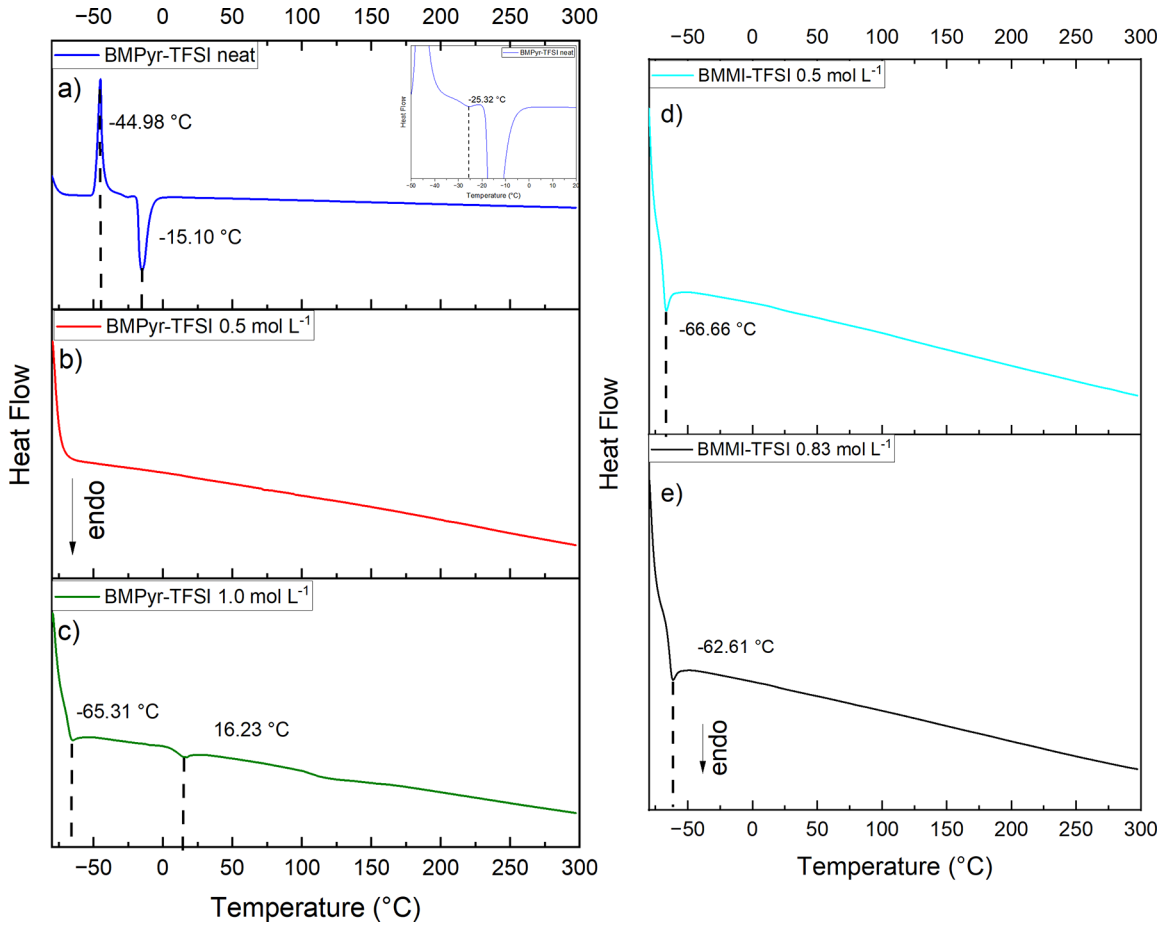

Figure 4. DSC patterns for the different ILs: (a) BMPyr-TFSI neat; (b) BMPyr-TFSI 0.5 mol L^{-1}; (c) BMPyr-TFSI 1.0 mol L^{-1}; (d) BMMI-TFSI 0.5 mol L^{-1}; (e) BMMI-TFSI 0.83 mol L^{-1}.

vs Na/Na^+ and remains in a prismatic structure. However, below 2.0 V vs Na/Na^+, a redox reaction occurs between the Mn^{3+}/Mn^{4+} redox couple, which can lead to lattice distortions in the electrode due to Jahn−Teller effect of Mn^{3+}.[86,87] The onset of a small potential plateau can be observed at about 2.5 V vs Na/Na^+ during the discharge and at around 2.6 V vs Na/Na^+ during charge. This plateau is associated with rearrangements between Na^+ and the host vacancies.[82] For currents above 34.5 mA g^{-1} (C/5), the absence of some plateaus is ascribed to increased polarization of the system.

Concerning the results with the IL mixtures (Figure 5b−e), the positive electrode exhibited a profile similar to that of the conventional electrolyte in the BMPyr-based ILs (Figure 5b,c) only at low rates (C/20), in contrast to the BMMI-based electrolytes (Figure 5d,e). For the latter, a more drastic change in the potential is observed during cycling at both salt concentrations, possibly associated with kinetic limitations due to the poorer transport properties of the $BMMI^+$ cation. This becomes more evident for currents higher than 8.65 mA g^{-1}.

The rate capability results shown in Figure 6 can better explain the cycling performance of NNM in the different electrolytes. The results show that NNM achieves its highest specific discharge capacity in the conventional $NaClO_4$ electrolyte (blue square), delivering a capacity of 61.2 mA h g^{-1} at C/20 rate. As previously mentioned, NNM has a theoretical capacity of 173 mA h g^{-1} when 2/3 mol of Na^+ is transferred. However, within the potential range investigated (2.5−4.0 V vs Na/Na^+), only one-third of the molar amount of Na^+ is involved in the electrochemical process,[13] explaining why the capacities are lower than the theoretical value. In this electrolyte, the NNM electrode presented similar performance at C/20, C/10, and C/5 rates, displaying specific discharge capacities of 61.2, 59.1, and 55.7 mA h g^{-1}, and a reversible capacity of 55.3 mA h g^{-1} at C/10 rate. This response can be related to the higher ionic conductivity of the electrolyte (7.8 mS cm^{-1})[88] compared to the ILs, as well as to its lower viscosity (6.0 mPa s).[89] Additionally, EC and PC present higher dielectric constants than typical organic solvents,[89] providing a higher degree of dissociation for $NaClO_4$ (86.2%).[89]

Among the ILs, BMPyr-TFSI containing 0.5 mol L^{-1} of NaTFSI (red square) showed the best cyclability and stability, achieving a discharge capacity of 40.0 mA h g^{-1} for the first cycle at C/10 and a capacity of 39.3 mA h g^{-1} for the second cycle at the same rate. BMPyr-TFSI with 1.0 mol L^{-1} of NaTFSI (green square) showed a lower capacity: 33.3 mA h g^{-1} at C/10 rate and a reversible capacity of 30.7 mA h g^{-1}. These differences can be ascribed to the better transport properties at lower salt concentrations.

In the case of BMMI-based electrolytes, NNM performed worse at 0.5 (cyan square) and 0.83 mol L^{-1} (black square) of NaTFSI for cycles above C/20 rate. However, comparing the physicochemical properties of the two families of ILs (Figure 2) with the same salt concentration (0.5 mol L^{-1}), the values are close and, therefore, a similar performance could have been expected. As discussed in the previous section, however, the

https://doi.org/10.1021/acs.jpcb.5c07871
J. Phys. Chem. B XXXX, XXX, XXX−XXX

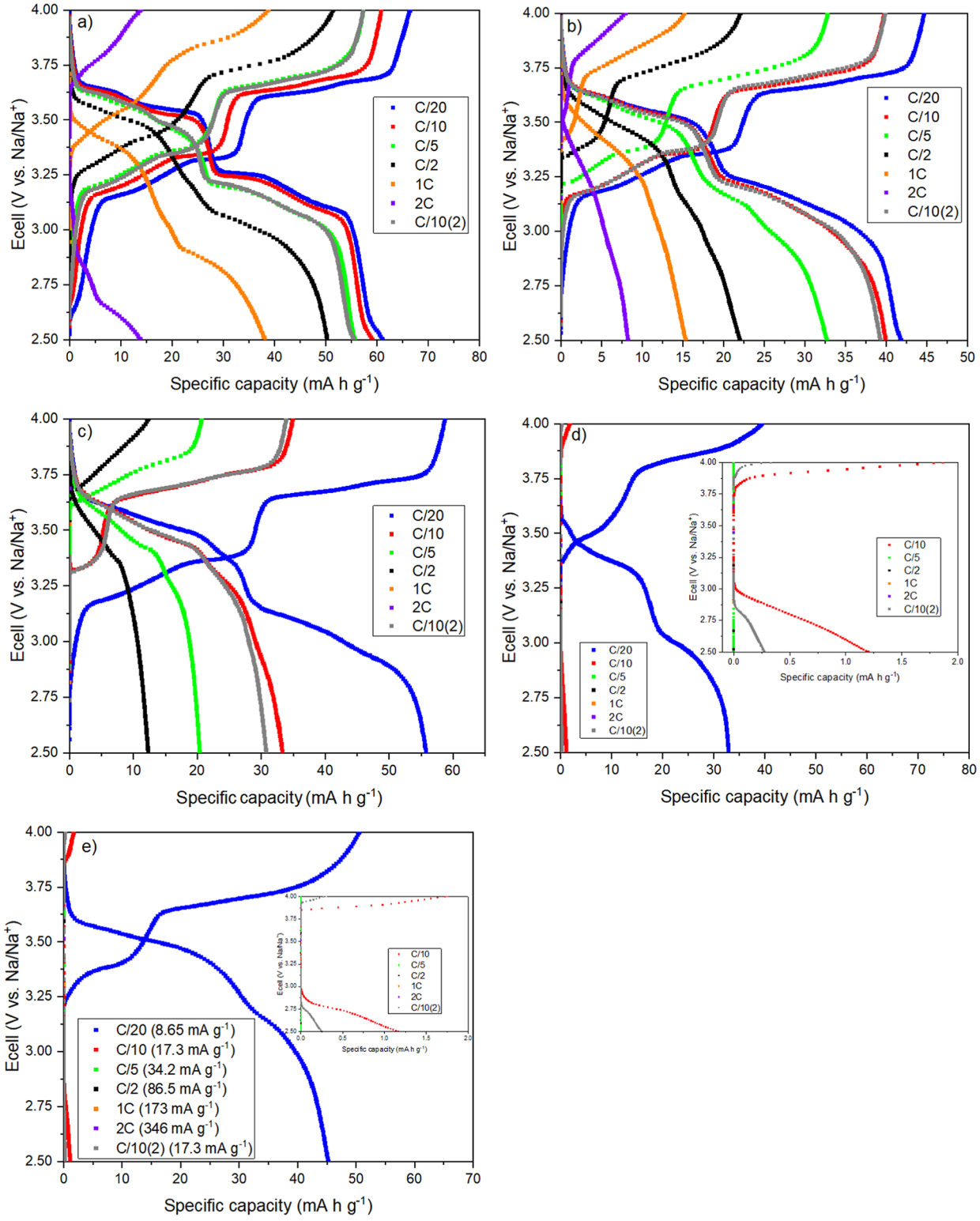

Figure 5. Potential profiles for the last cycle at each C-rate of Na-NNM batteries in the different electrolytes: (a) $NaClO_4$ 1.0 mol L^{-1} (EC/PC − 1:1); (b) BMPyr-TFSI 0.5 mol L^{-1}; (c) BMPyr-TFSI 1.0 mol L^{-1}; (d) BMMI-TFSI 0.5 mol L^{-1}; (e) BMMI-TFSI 0.83 mol L^{-1}.

$BMMI^+$ configuration favors ion−ion interactions that can form neutral aggregates. This reduces the ionicity of IL mixtures and impairs the electrode performance. As the current density increases, the lower ionicity of the imidazolium-based electrolytes appears to significantly impact the cyclability of the electrode at higher C-rates.

The results for the IL-based electrolytes suggest kinetic limitations. To overcome this drawback and further evaluate the feasibility of using $BMPyr^+$ and $BMMI^+$ as electrolytes, galvanostatic cycles were carried out at very low current densities. For this purpose, the different IL mixtures were subjected to galvanostatic charge−discharge cycles at lower C-rates: C/100, C/50, and C/20. Figure 7 shows the potential

https://doi.org/10.1021/acs.jpcb.5c07871
J. Phys. Chem. B XXXX, XXX, XXX−XXX

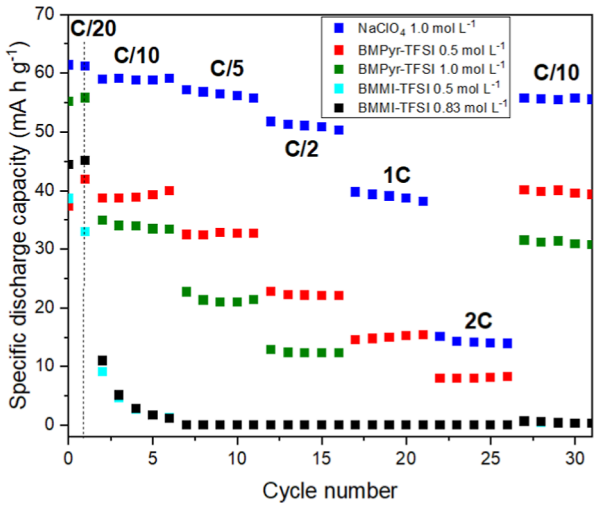

Figure 6. Rate capability of Na-NNM electrodes in the different electrolytes.

profiles for the positive electrode in the various ILs under these conditions. The respective specific currents are presented in the plot legend. The profile for the conventional electrolyte in the last C/20 cycle is also presented (Figure 7e). Table 2 shows the specific discharge capacities obtained from the NNM charge/discharge curves (Figure 7a–d). Additionally, the differential capacity plots (dQ/dE vs E) obtained from the last cycle at the three different rates are presented in Figure 8: C/20 (Figure 8a), C/50 (Figure 8b), and C/100 (Figure 8c), together with the result obtained at C/20 (last cycle) for the conventional organic electrolyte. Although dQ/dE vs E is commonly used to diagnose the state of health of a battery,[90,91] this type of analysis is also interesting since it provides the fingerprint of the battery system. On the dQ/dE vs E diagrams, each plateau in the potential profile corresponds to a peak, which can be associated with phase changes and intercalation/deintercalation phenomena during the battery cycling.[83,92]

The four potential plateaus for NNM in the conventional $NaClO_4$ electrolyte (Figure 7e) are reflected by peaks in the dQ/dE versus E plots (blue curve in Figure 8). In addition, a small plateau below 3.0 V vs Na/Na^+, which is associated with the order rearrangements between Na^+ and the host vacancies,[82] is evident as a small shoulder in the dQ/dE vs E plots (indicated by the red arrows). Results for the IL-based electrolytes (Figure 7a–d) show that the cycling rate plays an important role in battery performance. Decreasing the current density resulted inthe electrodes exhibiting a profile similar to that of the conventional electrolyte at C/20. Discharge capacities above 50 mAh g^{-1} were observed at C/100 and C/50 for all conditions (Table 2). Furthermore, the differential capacity plots for both IL families at these rates (Figure 8b,c) show the same four well-defined peaks as in the diagram for the conventional electrolyte. However, compared with perchlorate, potential shifts are observed for the peaks during charge and discharge with increasing C-rate from C/100 to C/50 (positions indicated by the red and black dashed lines, respectively), which can be attributed to increased battery polarization. At C/20 rate, a drastic drop in potential is observed for the ILs during the discharge cycle, resulting in the absence of the characteristic peaks below 3.25 V vs Na/Na^+ (Figure 8a). This behavior is mainly associated with overpotential due to mass transport limitation.[13]

Similar behavior and close capacity values were observed for all mixtures of BMMI- and BMPyr-based electrolytes at very low rates (C/100 and C/50) (Table 2). These similarities can be attributed to the restricted potential range used in the study, which limits the maximum amount of Na^+ that can be transferred. Conversely, at C/20 rate, NNM showed a better response in BMPyr-TFSI with 0.5 mol L^{-1} NaTFSI (Figure 7a), compared to BMMI-TFSI with the same salt concentration (Figure 7c), probably due to the better transport properties of the pyrrolidinium cation. The electrode also showed better performance with electrolytes containing higher salt concentrations, i.e., BMPyr-TFSI and BMMI-TFSI with 1.0 mol L^{-1} and 0.83 mol L^{-1} NaTFSI (Figure 7b,d, respectively). This behavior is consistent with the results observed for the rate capability experiments presented in Figure 5, and may be linked to the availability of charge carriers and the sufficiently low reaction rate that allows Na^+ ions to intercalate.

Figure 9 shows the rate capability (a) and the Coulombic efficiency (CE) (b) versus the number of cycles for NNM in the IL mixtures cycled at low C-rates. Under these conditions, the electrode capacity and cyclability improve for both IL families, resulting in a more stable behavior at C/50 (Figure 9a). Moreover, after five cycles, the CEs were about 98.6 and 98.1% for BMPyr-TFSI with 0.5 and 1.0 mol L^{-1} NaTFSI, and 96.3 and 98.3% for BMMI-TFSI with 0.5 and 0.83 mol L^{-1} NaTFSI (Figure 9b). For the positive electrode, CE is the ratio of discharge to charge capacities, indicating the battery's reversibility, which should be close to 100%. Several factors can reduce the CE, including electrolyte stability, the solid electrolyte interphase properties, the working potential, and the irreversibility of the desodiation/sodiation process, among others.[93,94]

The CEs for NNM in the conventional electrolyte at different C-rates (Figure S5) also show variations over the cycles. After the final cycles at C/10, C/5, C/2, 1C, and 2C, corresponding to the fifth cycle, the CEs were around 97.1, 97.2, 97.7, 98.0, and 99.6%, respectively. These values were compared with those reported by Liu et al.,[37] whose efficiencies were estimated from potential profiles (range 2.0–4.0 V vs Na/Na^+) for the active material synthesized at 850 °C. The CEs reported by Liu et al.[37] were even lower than those found in the present study. After 20 cycles at C/10, C/5, C/2, 1C, and 2C, the efficiencies were estimated around 94.1, 94.1, 94.7, 96.9, and 94.1%, respectively, indicating a certain degree of irreversibility of the synthesized electrode.

For the NNM cycled at C/20 (Figure 9a), the battery capacity drops in all IL mixtures, with the BMMI-TFSI mixtures containing 0.5 and 0.83 mol L^{-1} NaTFSI showing the most pronounced drop. This result is in agreement with those presented in Figure 6, which show that NNM displays a better performance in the BMPyr-based mixtures than in the BMMI-based ones. Nevertheless, a reduction in CEs was observed for all electrolytes with increasing number of cycles for this faster cycling. For instance, after five cycles, NNM reached CEs around 94.5% and 92.2% for BMPyr-TFSI with 0.5 and 1.0 mol L^{-1} NaTFSI, and 88.0% and 92.3% for BMMI-TFSI with 0.5 and 0.83 mol L^{-1} NaTFSI. These decreases may be associated with increased internal resistance and self-consumption.[95,96]

The results discussed in this section demonstrate a clear relationship between the current density of a cycle and the performance of the electrolytes. In fact, kinetic limitations

https://doi.org/10.1021/acs.jpcb.5c07871
J. Phys. Chem. B XXXX, XXX, XXX−XXX

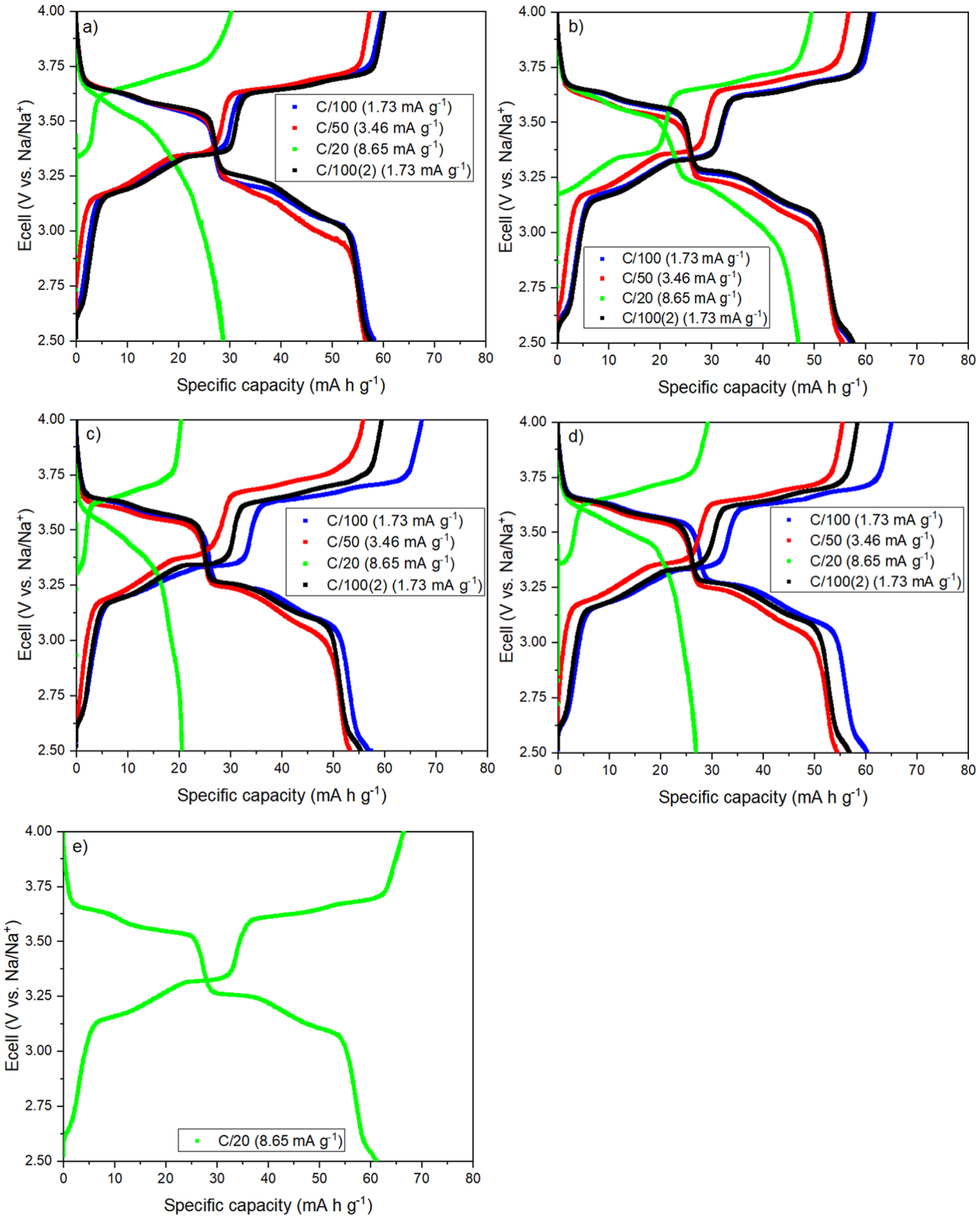

Figure 7. Potential profiles for the last cycle at each C-rate of Na-NNM batteries in the different IL mixtures: (a) BMPyr-TFSI 0.5 mol L^{-1}; (b) BMPyr-TFSI 1.0 mol L^{-1}; (c) BMMI-TFSI 0.5 mol L^{-1}; (d) BMMI-TFSI 0.83 mol L^{-1}; (e) $NaClO_4$ 1.0 mol L^{-1} (EC/PC—1/1) last cycle at C/20.

arising from IL transport properties can be overcome by lowering the C-rate. Remarkably, comparable performance of both nitrogen-based ILs to the perchlorate-based electrolyte in terms of Coulombic efficiency and capacity establishes BMPyr-TFSI and BMMI-TFSI ILs as promising electrolytes for NNM. Nevertheless, to understand and evaluate their actual applicability as possible substitutes for the conventional system, electrochemical performance and stability over more extended cycling periods are necessary and will be addressed in future studies.

https://doi.org/10.1021/acs.jpcb.5c07871
J. Phys. Chem. B XXXX, XXX, XXX−XXX

Table 2. Specific Discharge Capacities Obtained From the Potential Profiles at the C-Rates Presented in Figure 7

cation−anion pair	NaTFSI concentration (mol L^{-1})	specific discharge capacities (mA h g^{-1}) C/100	C/50	C/20	C/100
BMPyr-TFSI	0.5	58.24	56.53	28.72	57.78
	1.0	57.21	55.68	47.40	57.61
BMMI-TFSI	0.5	57.49	53.79	20.54	55.38
	0.83	60.33	54.54	26.93	56.83

Sodium Diffusion Coefficient Determination

Given that only the portion of current carried by sodium ions is relevant in SIBs, and considering that the intercalation process depends fundamentally on this species, it is important that the metal cation demonstrates adequate diffusivity in the electrolyte. Therefore, in addition to the physicochemical properties of ILs, a crucial parameter in the proposal of new electrolytes for sodium-based systems is the diffusion coefficient of Na^+. As illustrated in Figures S6 and S7, galvanostatic curves and Nyquist diagrams were employed to estimate the sodium diffusion coefficient (D_{Na^+}). For the extraction of D_{Na^+} values, the electrochemical response was expressed in terms of the faradaic impedance (Z_f), represented by the sum of the charge transfer resistance (R_{ct}) and the Warburg impedance (Z_w), as shown in eq 3.[97,98]

$$Z_f = R_{ct} + Z_w \tag{3}$$

Z_w contribution can be expressed as follows (eq 4):[98]

$$Z_w = \frac{R \times T}{n^2 \times F^2 \times \sqrt{j\omega}}\left(\frac{1}{\sqrt{D_{ox} \times C_{ox}(0)}} + \frac{1}{\sqrt{D_{red} \times C_{red}(0)}}\right) \tag{4}$$

In eq 4, R is the ideal gases constant (8.314 J mol^{-1} K^{-1}), T the absolute temperature (K), in this case room temperature (298 K), n the number of electrons transferred, F the Faraday constant (96,485 C mol^{-1}), D_{ox} and D_{red} correspond to the diffusion coefficients (cm^2 s^{-1}) of the oxidized and reduced species, respectively, while $C_{ox}(0)$ and $C_{red}(0)$ stand for the concentration (mol cm^{-3}) of the oxidized and reduced species on the electrode surface. Assuming that surface concentrations obey the Nernst law, it is possible to rearrange the Nernst equation and express the ratio $C_{ox}(0)/C_{red}(0)$ in terms of eq 5.

$$\frac{C_{ox}(0)}{C_{red}(0)} = e^{\left(\frac{n\times F}{R\times T}\times(E-E^0)\right)} \tag{5}$$

E represents the electrode potential (V) and E^0 the equilibrium potential (V). It is posited that if the diffusivities of the oxidized and reduced species are equal, the Nernst Equation can be rewritten in terms of the half-wave potential ($E_{1/2}$), as shown in eq 6:[99]

$$E_{1/2} = E^0 + \frac{R \times T}{n \times F} \times \ln\left(\sqrt{\frac{D_{red}}{D_{ox}}}\right) \tag{6}$$

By replacing eqs 5 and 6 in eq 4, the equation for the diffusion impedance can be rewritten (eq 7)

$$Z_w = \frac{4 \times R \times T}{n^2 \times F^2 \times C_{ox} \times \sqrt{j\omega \times D_{ox}}} \cosh^2\left(\frac{n \times F \times (E - E_{1/2})}{2 \times R \times T}\right) \tag{7}$$

For a finite length linear diffusion, the boundary conditions for solving the second Fick's law are adapted, thus eq 7 turns to eq 8

$$Z_w = \frac{R \times T}{n^2 \times F^2 \times \sqrt{j\omega}}\left(\frac{\coth\left(\delta_N \times \sqrt{\frac{j\omega}{D_{ox}}}\right)}{\sqrt{D_{ox} \times C_{ox}(0)}} + \frac{\coth\left(\delta_N \times \sqrt{\frac{j\omega}{D_{red}}}\right)}{\sqrt{D_{red} \times C_{red}(0)}}\right) \tag{8}$$

δ_N represents the diffusion layer thickness. As the diffusivities of the oxidized and reduced species are equals ($D_{ox} = D_{red} = D$), eq 8 can be reduced to eq 9

$$Z_w = \frac{4 \times R \times T}{n^2 \times F^2 \times C_{ox} \times \sqrt{D}} \cosh^2\left(\frac{n \times F \times (E - E_{1/2})}{2 \times R \times T}\right)\left(\frac{\coth\left(\delta_N \times \sqrt{\frac{j\omega}{D}}\right)}{\sqrt{j\omega}}\right) \tag{9}$$

For describing a nonideal behavior of the diffusion impedance, a parameter similar to a CPE that accounts for such response, represented by the symbol (Φ_w), can be introduced in eq 9,[100,101] resulting in eq 10

$$Z_w = \frac{4 \times R \times T}{n^2 \times F^2 \times C_{ox} \times \sqrt{D}} \cosh^2\left(\frac{n \times F \times (E - E_{1/2})}{2 \times R \times T}\right) \frac{\delta_N}{\sqrt{D} \times \left(\delta_N \times \sqrt{\frac{j\omega}{D}}\right)^{\Phi_w}} \coth\left(\delta_N \times \sqrt{\frac{j\omega}{D}}\right)^{\Phi_w} \tag{10}$$

To fit the experimental data, the Measurement Model software was used.[102] The fitting results, as well as the parameters, are presented in the SI section (Figure S8 and Table S3). Table 3 shows the D_{Na^+} estimations for the different electrolytes. For the perchlorate-based electrolyte, D_{Na^+} was estimated at 1.3×10^{-7} cm^2 s^{-1}. Since most studies on metallic ion diffusion in electrolytes for metal-ion systems are usually based on the use of pulsed field gradient (PEG)-NMR measurements,[103−106] resulting in values associated with the self-diffusion of the species,[103] a direct comparison between the values presented in Table 3 with those reported in the literature becomes quite challenging. However, through molecular dynamics simulations for 1.0 mol L^{-1} $NaClO_4$ in EC electrolyte, Friedman[107] estimated a Na^+ diffusion coefficient of 2.9×10^{-7} cm^2 s^{-1}, a value close to that found in the present work.

Concerning the ILs mixtures, the increase of NaTFSI concentration reduced the diffusivity of Na^+. For BMPyr-TFSI with 0.5 mol L^{-1} of NaTFSI, the estimated sodium diffusion coefficient was 1.41×10^{-7} cm^2 s^{-1}, while for 1.0 mol L^{-1} the

https://doi.org/10.1021/acs.jpcb.5c07871
J. Phys. Chem. B XXXX, XXX, XXX−XXX

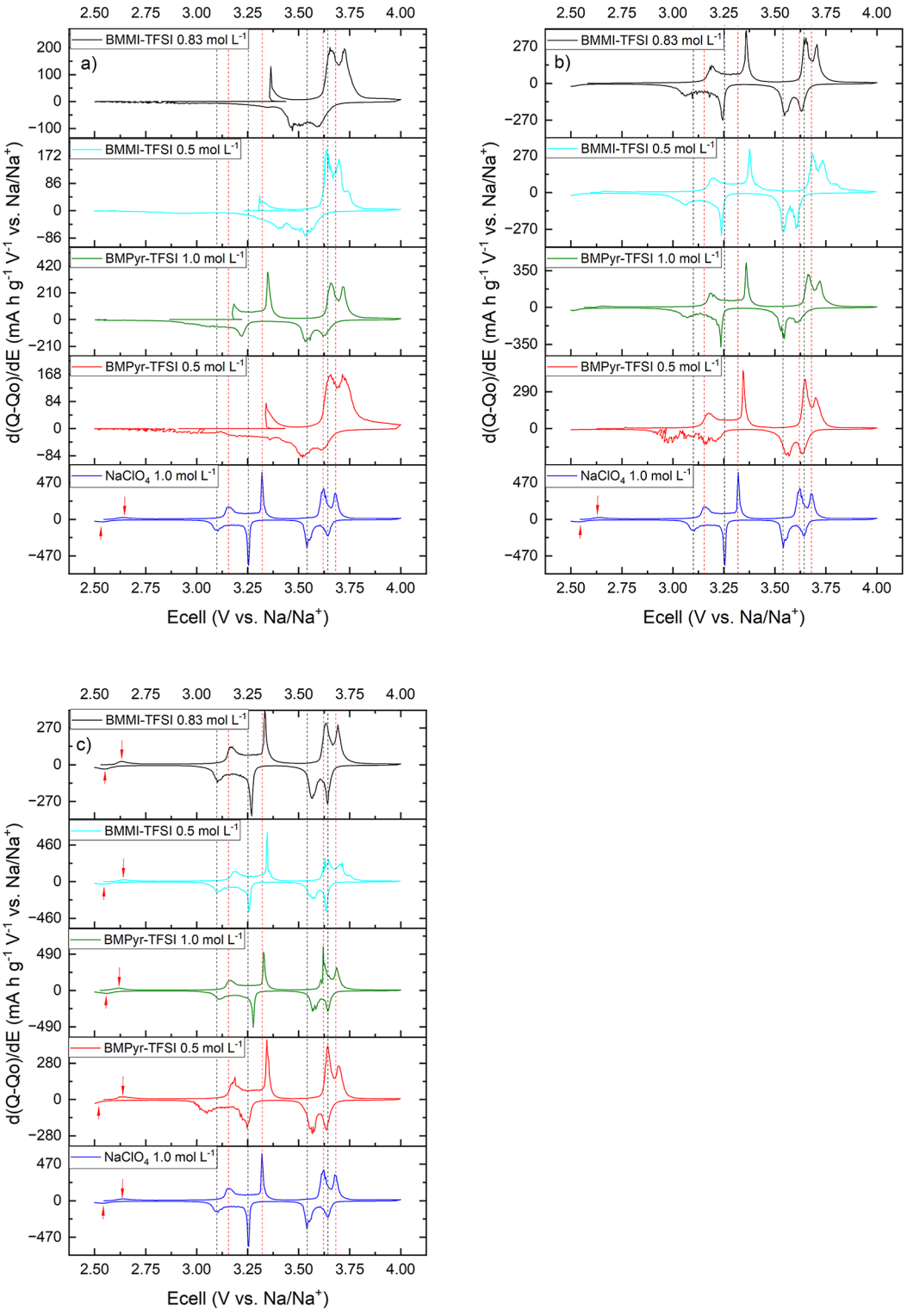

Figure 8. dQ/dE vs E curves for Na-NNM batteries at different rates: (a) C/20; (b) C/50; (c) C/100. In each set, the plot for $NaClO_4$ corresponds to the result obtained at the last cycle at C/20. The red dashed lines correspond to the potential shifts for the peaks of NNM in ILs mixture during charge, and the black ones to the potential shifts for the peaks of NNM in ILs mixture during discharge, both compared to the positions in the conventional electrolyte.

value was almost 2.5 times lower (5.55×10^{-8} cm^2 s^{-1}). In the case of imidazolium-based electrolytes, the estimated diffusion coefficient for BMMI-TFSI with 0.5 and 0.83 mol L^{-1} of NaTFSI were 2.7×10^{-7} and 1.83×10^{-8} cm^2 s^{-1}, respectively. These observations are in agreement with previous studies that reported analogous behaviors in the presence of varying concentrations of metallic salts in ILs.[68,71,108,109] These studies attributed this behavior to alterations in solvation dynamics, due to the elevated NaTFSI content.[71] Although higher salt concentrations have been shown to increase the metallic cation transfer number,[110] defined as the proportion of the total current carried by the metallic ion, this increase in the density

https://doi.org/10.1021/acs.jpcb.5c07871
J. Phys. Chem. B XXXX, XXX, XXX−XXX

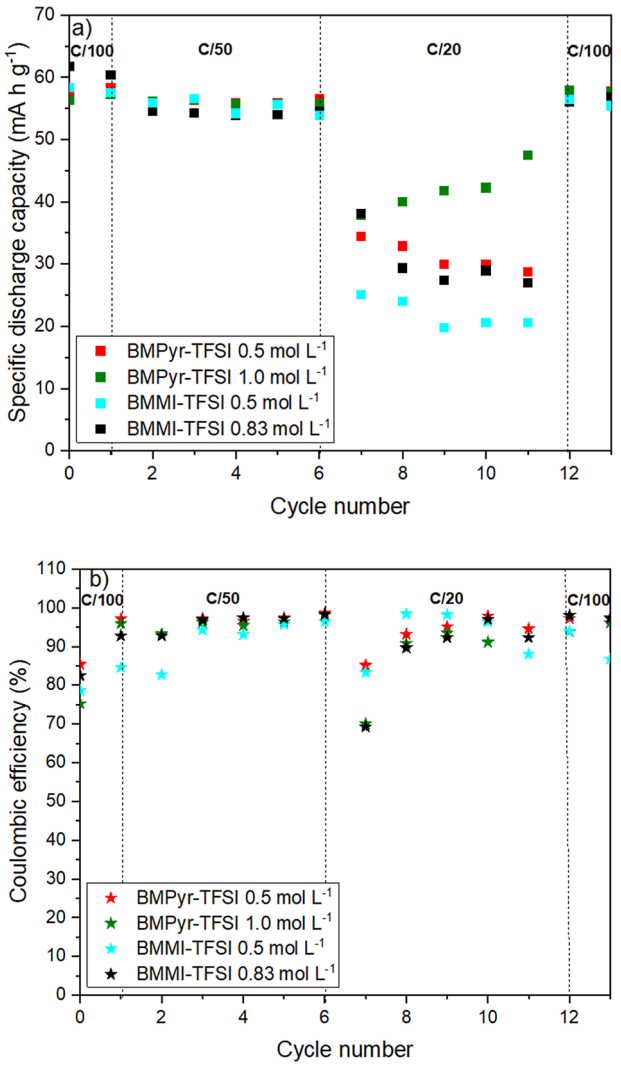

Figure 9. Performance of Na-NNM electrodes in the different electrolytes at low C-rates: (a) rate capability; (b) Coulombic efficiency.

Table 3. Sodium Diffusion Coefficients Calculated from eq 3

electrolyte	salt concentration (mol L^{-1})	sodium diffusion coefficient (cm^2 s^{-1})
$NaClO_4$ in EC/PC (1:1 v/v)	1.0	1.30×10^{-7}
BMPyr-TFSI	0.5	1.41×10^{-7}
	1.0	5.55×10^{-8}
BMMI-TFSI	0.5	2.70×10^{-7}
	0.83	1.83×10^{-8}

of ionic species leads to an increase in Na-TFSI interactions, as previously discussed in the section on physicochemical properties of ILs. The increase in Na-TFSI interactions explains the inhibition of sodium mobility at higher NaTFSI concentrations. A comparison of the diffusion coefficient values estimated in the ILs containing $BMPyr^+$ and $BMMI^+$ at the same salt concentration (0.5 mol L^{-1} of NaTFSI), suggests that a larger difference between the D_{Na^+} values would be expected, especially considering the overall superior cycling performance shown by NNM in the BMPyr-TFSI IL at higher C-rates (Figures 5 and 6). However, the efficiency of an electrolyte depends not only on the diffusivity of charge carriers through the medium, but also on the density of carriers available for diffusion. As illustrated by the Walden's plot (Figure 3), for a concentration of 0.5 mol L^{-1} of NaTFSI, the density of aggregates formed in the imidazolium-based IL is greater than that observed in the pyrrolidinium-based electrolyte. Thus, despite the physicochemical properties of the two mixtures being analogous, the enhanced tendency to form aggregates in the presence of $BMMI^+$ seems to play a significant role, influencing the performance of the electrolyte.

CEI Properties

In addition to considerations of battery stability and cyclability, the solid electrolyte interphase formed between the cathode and the electrolyte plays a crucial role. This interphase obstructs the electronic transport of the active material to the electrolyte while allowing the passage of metal cations during intercalation and deintercalation.[111] Moreover, it modulates the reaction rate in the battery.[112] One way to access information about the properties of the CEI is through the EIS technique, in which it is possible to discriminate the contribution of this passive film in relation to other systems for the electrochemical response of the battery.

Figure 10 shows the Nyquist plots obtained prior to and following cycling in the different electrolytes. After cycling, the spectra were obtained at the discharged state of the NNM electrode, i.e., at 2.5 V vs Na/Na^+. For the conventional electrolyte (Figure 10a), the diagram prior to cycling can be decrypted into two regions. In the high-to-medium frequency range (10 kHz−10 Hz), the semicircle is indicative of Na^+ transfer across the interface between the active material surface and the electrolyte,[113] mainly associated with charge-transfer resistance.[114,115] At lower frequencies (below 2 Hz), the response of the system becomes more resistive, which could indicate limitations in mass transfer. After the two cycles at C/20 (illustrated by the filled blue curve), an improvement in the electrode response was observed, accompanied by a decrease in impedance, possibly related to the formation of a stable CEI. Previous works[89,116] on the use of different organic solvents combinations for Na-ion batteries have also shown that the combination of EC/PC as a solvent for $NaClO_4$ enhances battery performance, attributed to the formation of a solid interphase with superior properties.

In contrast with the perchlorate-based electrolyte, the NNM tested in the IL mixtures (Figure 10b−e) exhibited an overall increase in impedance after the two cycles at C/50. This response will be further discussed in the following paragraph. The analysis of the spectra showed a semicircle from high to medium frequencies, followed by a depressed arc at the low-frequency domain (below 1 Hz). This latter finding indicates a deviation from the ideal Warburg impedance, which is likely attributable to a diffusion-controlled process in bounded or irregular geometries.[117,118] Moreover, increasing the salt concentration of the ILs slightly increased the cell impedance, likely attributable to the electrolytes' poorer transport properties.

Figure 10f provides a comparison of the Nyquist plots for NNM after cycling in the various electrolytes. The positive electrode demonstrated the lowest impedance in perchlorate-based electrolyte (blue square curve), in contrast to all batteries tested in the ILs mixtures, which exhibited higher impedances. Do et al.[119] also performed EIS experiments to gather information on the properties of the P2−

https://doi.org/10.1021/acs.jpcb.5c07871
J. Phys. Chem. B XXXX, XXX, XXX−XXX

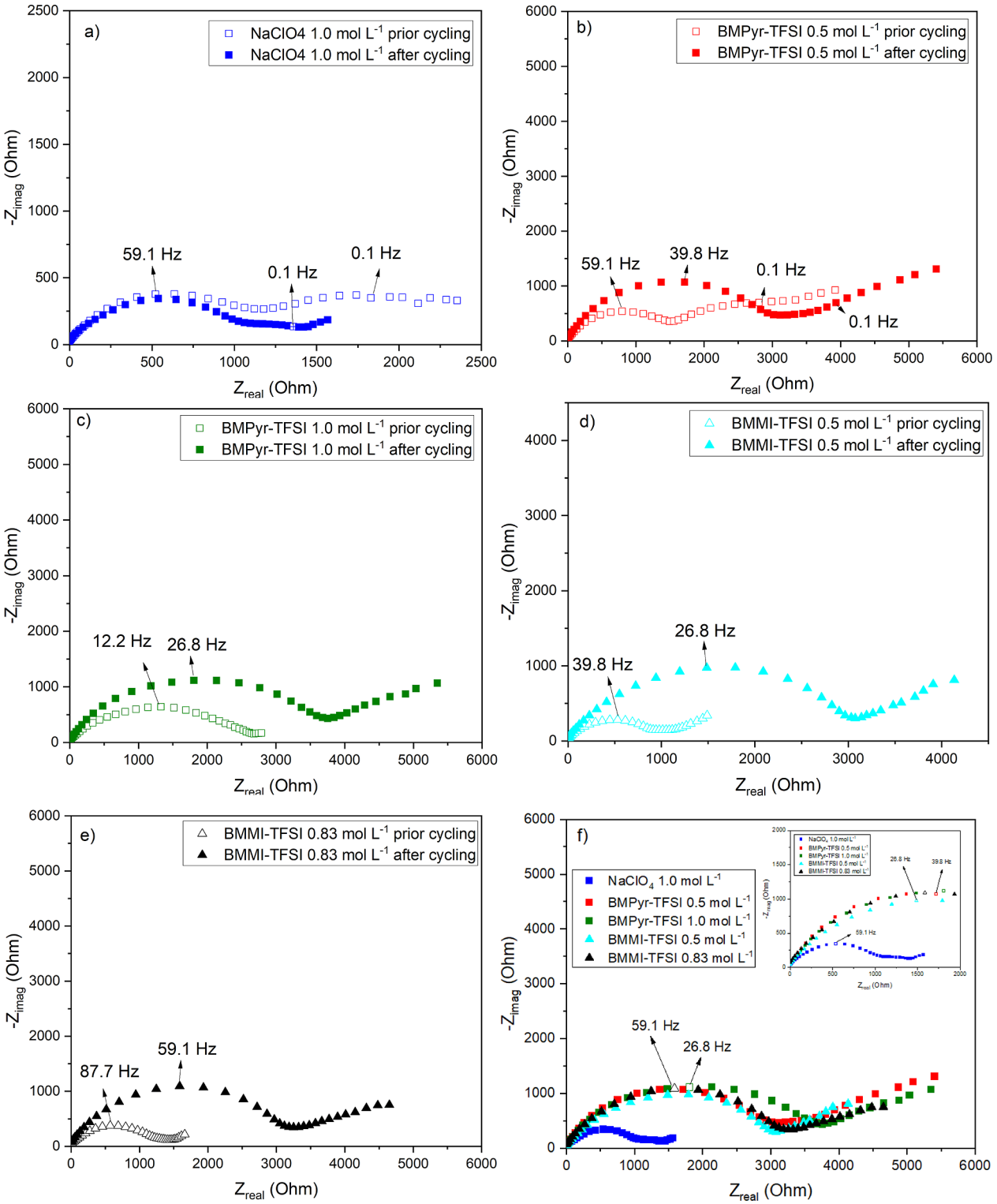

Figure 10. Nyquist plots obtained in the different electrolytes prior to and after cycling: (a) $NaClO_4$ 1.0 mol L^{-1}; (b) BMPyr-TFSI 0.5 mol L^{-1}; (c) BMPyr-TFSI 1.0 mol L^{-1}; (d) BMMI-TFSI 0.5 mol L^{-1}; (e) BMMI-TFSI 0.83 mol L^{-1}; (f) comparison between the different electrolytes after cycling.

$Na_{0.6}Co_{0.1}Mn_{0.9}O_{2+z}$ positive electrode, as well as the formed CEI, both in the 1.0 mol L^{-1} $NaClO_4$ in EC/PC and in the 0.5 mol L^{-1} NaTFSI in BMPyr-TFSI electrolytes. The EIS spectra were recorded after the first, 30th, and 500th galvanostatic charge−discharge cycle. While the response was better in $NaClO_4$ after 30 cycles, a decrease in impedance was observed between the first and the 30th cycle for the electrode tested in the IL. The authors suggested that this behavior may result from insufficient electrode wetting by the electrolyte or the formation of a more conductive CEI during the initial cycles. However, it is important to note that, in the present study, cycling was carried out at very low specific currents (3.46 mA

https://doi.org/10.1021/acs.jpcb.5c07871
J. Phys. Chem. B XXXX, XXX, XXX−XXX

g^{-1} compared to 50 mA g^{-1} in Do et al.), which would favor better electrode wetting by the electrolytes. Therefore, the observed impedance increase in all mixtures could be indicative of the formation of a CEI with more resistive characteristics than that formed in the conventional electrolyte. The formation of this passive layer is primarily attributed to the decomposition of IL anion,[119,120] suggesting that the chemical composition, as well as the final properties, will be similar for the different mixtures, thus explaining the comparable responses observed in Figure 10f for the ILs.

CONCLUSIONS

The electrochemical performance of two families of nitrogen-based ILs as electrolytes for the $Na_{0.67}Ni_{0.33}Mn_{0.67}O_2$ (NNM) positive electrode for sodium−ion batteries (SIBs) was evaluated. To supplement the existing body of knowledge, the physicochemical (density, viscosity, and conductivity) and thermal properties of the neat electrolytes and their mixtures with different concentrations of NaTFSI were determined and compared. Among the neat ILs, BMPyr-TFSI exhibited superior physicochemical properties, with higher conductivity and lower viscosity compared to BMMI-TFSI. Furthermore, the addition of salt was detrimental to the electrolyte properties, resulting in increased density and viscosity while concurrently reducing the ionic conductivity.

Concerning the electrochemical behavior, galvanostatic cycling results demonstrated that, when cycled at high rates (above C/20), the NNM positive electrode showed significantly worse behavior in the ILs when compared with the conventional electrolyte ($NaClO_4$). Moreover, the EIS experiments indicated the potential formation of a CEI with enhanced resistive characteristics in the presence of the IL mixtures, which could impede the intercalation/deintercalation process of the metal cation. A reduction in current density (C/50 and C/100) has been shown to enhance the performance of the IL-based electrolytes, apparently suppressing the kinetic limitations due to poorer transport properties. At these low rates, both pyrrolidinium and imidazolium-based ILs showed capacities and efficiencies comparable to those of the perchlorate-based electrolyte, suggesting they may be suitable alternatives as safe electrolytes.

ASSOCIATED CONTENT

Supporting Information

The Supporting Information is available free of charge at https://pubs.acs.org/doi/10.1021/acs.jpcb.5c07871.

The X-ray diffraction pattern for the pristine NNM particles is presented in Figure S1. Figures S2 and S3 present the SEM image of the electrode prior to the experiments (backscattered electrons) and the EDS spectrum of the NNM particles, respectively. Figure S4 shows the linear representation of the Walden plot for the different mixtures of nitrogen-based ILs. Table S1 presents the parameters obtained from the viscosity curves fitting with VFT eq (1), and Table S2 shows the parameters obtained from the conductivity curves fitting with the VFT eq (2). Figure S5 presents the Coulombic efficiency of NNM in 1.0 mol L^{-1} $NaClO_4$ (EC/PC) at different C-rates. Figure S6 presents the galvanostatic cycles of sodium deposition on copper electrodes prior to the acquisition of EIS spectra. Figure S7 shows the impedance spectra after galvanostatic treatment. The fitting results for the extraction of sodium diffusion coefficients, in the different electrolytes, from experimental impedance data are presented in Figure S8. Table S3 shows the parameters obtained for the fitting of the EIS diagrams (PDF)

AUTHOR INFORMATION

Corresponding Authors

Mireille Turmine − *Laboratoire de Réactivité de Surface (LRS), Sorbonne Université, CNRS, Paris 75005, France;* orcid.org/0000-0002-5939-5065; Email: mireille.turmine@sorbonne-universite.fr

Vitor L. Martins − *Departamento de Química Fundamental, Instituto de Química, Universidade de São Paulo, São Paulo, São Paulo 05508-000, Brazil;* orcid.org/0000-0002-8824-7328; Email: martinsv@usp.br

Hercilio G. de Melo − *Departamento de Engenharia Metalúrgica e de Materiais, Universidade de São Paulo, São Paulo, São Paulo 05508-030, Brazil;* orcid.org/0000-0002-9116-681X; Email: hgdemelo@usp.br.

Authors

Leandro S. Domingues − *Departamento de Engenharia Metalúrgica e de Materiais, Universidade de São Paulo, São Paulo, São Paulo 05508-030, Brazil; Laboratoire de Réactivité de Surface (LRS), Sorbonne Université, CNRS, Paris 75005, France;* orcid.org/0000-0002-5287-5306

Roberto M. Torresi − *Departamento de Química Fundamental, Instituto de Química, Universidade de São Paulo, São Paulo, São Paulo 05508-000, Brazil;* orcid.org/0000-0003-4414-5431

Vincent Vivier − *Laboratoire de Réactivité de Surface (LRS), Sorbonne Université, CNRS, Paris 75005, France;* orcid.org/0000-0001-5424-0083

Complete contact information is available at: https://pubs.acs.org/10.1021/acs.jpcb.5c07871

Author Contributions

The manuscript was written with the contributions of all authors. All authors have approved the final version of the manuscript.

Funding

Leandro Souza Domingues thanks CAPES (88887.484841/2020-00) and CNPQ (200839/2022-5) for the scholarships. The Article Processing Charge for the publication of this research was funded by the Coordenacao de Aperfeicoamento de Pessoal de Nivel Superior (CAPES), Brazil (ROR identifier: 00x0ma614).

Notes

The authors declare no competing financial interest.

ACKNOWLEDGMENTS

The authors are in debt with Coordenação de Aperfeiçoamento de Pessoal de Nível Superior—Brasil (CAPES, Finance Code 001) and FAPESP (2019/26309-4 and 2021/00675-4) for financial support. This study was financed in part by the National Council for Scientific and Technological Development − CNPq (Process: 200839/2022-5).

REFERENCES

(1) Larcher, D.; Tarascon, J. M. Towards Greener and More Sustainable Batteries for Electrical Energy Storage. *Nat. Chem.* **2015**, *7* (1), 19−29.

(2) Mamalis, A. G.; Spentzas, K. N.; Mamali, A. A. The Impact of Automotive Industry and Its Supply Chain to Climate Change: Somme Techno-Economic Aspects. *Eur. Transp. Res. Rev.* **2013**, *5* (1), 1−10.

(3) Mohd Noor, S. A.; Howlett, P. C.; Macfarlane, D. R.; Forsyth, M. Properties of Sodium-Based Ionic Liquid Electrolytes for Sodium Secondary Battery Applications. *Electrochim. Acta* **2013**, *114*, 766−771.

(4) Kumar, K.; Kundu, R. Empowering Energy Storage Technology: Recent Breakthroughs and Advancement in Sodium-Ion Batteries. *ACS Appl. Energy Mater.* **2024**, *7*, 3523−3539.

(5) Vera, M. L.; Torres, W. R.; Galli, C. I.; Chagnes, A.; Flexer, V. Environmental Impact of Direct Lithium Extraction from Brines. *Nat. Rev. Earth Environ.* **2023**, *4*, 149−165.

(6) Kim, S. W.; Seo, D. H.; Ma, X.; Ceder, G.; Kang, K. Electrode Materials for Rechargeable Sodium-Ion Batteries: Potential Alternatives to Current Lithium-Ion Batteries. *Adv. Energy Mater.* **2012**, *2*, 710−721.

(7) Ortiz-Vitoriano, N.; Drewett, N. E.; Gonzalo, E.; Rojo, T. High Performance Manganese-Based Layered Oxide Cathodes: Overcoming the Challenges of Sodium Ion Batteries. *Energy Environ. Sci.* **2017**, *10* (5), 1051−1074.

(8) Chen, T.; Ouyang, B.; Fan, X.; Zhou, W.; Liu, W.; Liu, K. Oxide Cathodes for Sodium-Ion Batteries: Designs, Challenges, and Perspectives. *Carbon Energy* **2022**, *4* (2), 170−199.

(9) Bommier, C.; Surta, T. W.; Dolgos, M.; Ji, X. New Mechanistic Insights on Na-Ion Storage in Nongraphitizable Carbon. *Nano Lett.* **2015**, *15* (9), 5888−5892.

(10) Mao, Q.; Gao, R.; Li, Q.; Ning, D.; Zhou, D.; Schuck, G.; Schumacher, G.; Hao, Y.; Liu, X. O3-Type NaNi0.5Mn0.5O2 Hollow Microbars with Exposed {0 1 0} Facets as High Performance Cathode Materials for Sodium-Ion Batteries. *Chem. Eng. J.* **2020**, *382* (June 2019), 122978.

(11) Zhao, C.; Yao, Z.; Wang, Q.; Li, H.; Wang, J.; Liu, M.; Ganapathy, S.; Lu, Y.; Cabana, J.; Li, B.; Bai, X.; Aspuru-Guzik, A.; Wagemaker, M.; Chen, L.; Hu, Y. S. Revealing High Na-Content P2-Type Layered Oxides as Advanced Sodium-Ion Cathodes. *J. Am. Chem. Soc.* **2020**, *142* (12), 5742−5750.

(12) Palomares, V.; Serras, P.; Villaluenga, I.; Hueso, K. B.; Carretero-González, J.; Rojo, T. Na-Ion Batteries, Recent Advances and Present Challenges to Become Low Cost Energy Storage Systems. *Energy Environ. Sci.* **2012**, *5* (3), 5884−5901.

(13) Mao, J.; Liu, X.; Liu, J.; Jiang, H.; Zhang, T.; Shao, G.; Ai, G.; Mao, W.; Feng, Y.; Yang, W.; Liu, G.; Dai, K. P2-Type Na 2/3 Ni 1/3 Mn 2/3 O 2 Cathode Material with Excellent Rate and Cycling Performance for Sodium-Ion Batteries. *J. Electrochem. Soc.* **2019**, *166* (16), A3980−A3986.

(14) Yoshida, H.; Yabuuchi, N.; Kubota, K.; Ikeuchi, I.; Garsuch, A.; Schulz-Dobrick, M.; Komaba, S. P2-Type Na2/3Ni1/3Mn2/3−xTixO2 as a New Positive Electrode for Higher Energy Na-Ion Batteries. *Chem. Commun.* **2014**, *50* (28), 3677−3680.

(15) Yuan, D.; Hu, X.; Qian, J.; Pei, F.; Wu, F.; Mao, R.; Ai, X.; Yang, H.; Cao, Y. P2-Type Na0.67Mn0.65Fe0.2Ni 0.15O2 Cathode Material with High-Capacity for Sodium-Ion Battery. *Electrochim. Acta* **2014**, *116*, 300−305.

(16) Wu, X.; Guo, J.; Wang, D.; Zhong, G.; McDonald, M. J.; Yang, Y. P2-Type Na0.66Ni0.33-XZnxMn0.67O2 as New High-Voltage Cathode Materials for Sodium-Ion Batteries. *J. Power Sources* **2015**, *281*, 18−26.

(17) Hou, H.; Gan, B.; Gong, Y.; Chen, N.; Sun, C. P2-Type Na0.67Ni0.23Mg0.1Mn0.67O2 as a High-Performance Cathode for a Sodium-Ion Battery. *Inorg. Chem.* **2016**, *55* (17), 9033−9037.

(18) Doubaji, S.; Ma, L.; Asfaw, H. D.; Izanzar, I.; Xu, R.; Alami, J.; Lu, J.; Wu, T.; Amine, K.; Edström, K.; Saadoune, I. On the P2-NaxCo1-y(Mn2/3Ni1/3)YO2 Cathode Materials for Sodium-Ion Batteries: Synthesis, Electrochemical Performance, and Redox Processes Occurring during the Electrochemical Cycling. *ACS Appl. Mater. Interfaces* **2018**, *10* (1), 488−501.

(19) Hasa, I.; Passerini, S.; Hassoun, J. Toward High Energy Density Cathode Materials for Sodium-Ion Batteries: Investigating the Beneficial Effect of Aluminum Doping on the P2-Type Structure. *J. Mater. Chem. A Mater.* **2017**, *5* (9), 4467−4477.

(20) Morita, M.; Ishikawa, M.; Matsuda, Y. Organic Electrolytes for Rechargeable Lithium Ion Batteries. In *Lithium Ion Batteries Fundamental and Performance*; Wiley VCH: Tokyo, 1998; pp 156−180.

(21) Borah, R.; Hughson, F. R.; Johnston, J.; Nann, T. On Battery Materials and Methods. *Mater. Today Adv.* **2020**, *6*, 100046.

(22) Guo, F.; Hase, W.; Ozaki, Y.; Konno, Y.; Inatsuki, M.; Nishimura, K.; Hashimoto, N.; Fujita, O. Experimental Study on Flammability Limits of Electrolyte Solvents in Lithium-Ion Batteries Using a Wick Combustion Method. *Exp Therm Fluid Sci.* **2019**, *109*, 109858.

(23) Armand, M.; Endres, F.; MacFarlane, D. R.; Ohno, H.; Scrosati, B. Ionic-Liquid Materials for the Electrochemical Challenges of the Future. *Nat. Mater.* **2009**, *8* (8), 621−629.

(24) Martins, V. L.; Torresi, R. M. Ionic Liquids in Electrochemical Energy Storage. *Curr. Opin. Electrochem.* **2018**, *9*, 26−32.

(25) Bazito, F. F. C.; Kawano, Y.; Torresi, R. M. Synthesis and Characterization of Two Ionic Liquids with Emphasis on Their Chemical Stability towards Metallic Lithium. *Electrochim. Acta* **2007**, *52* (23), 6427−6437.

(26) Torimoto, T.; Tsuda, T.; Okazaki, K. I.; Kuwabata, S. New Frontiers in Materials Science Opened by Ionic Liquids. *Adv. Mater.* **2010**, *22* (11), 1196−1221.

(27) Risthaus, T.; Zhou, D.; Cao, X.; He, X.; Qiu, B.; Wang, J.; Zhang, L.; Liu, Z.; Paillard, E.; Schumacher, G.; Winter, M.; Li, J. A High-Capacity P2 Na2/3Ni1/3Mn2/3O2 Cathode Material for Sodium Ion Batteries with Oxygen Activity. *J. Power Sources* **2018**, *395* (March), 16−24.

(28) Lei, Z.; Chen, B.; Koo, Y. M.; Macfarlane, D. R. Introduction: Ionic Liquids. *Chem. Rev.* **2017**, *117* (10), 6633−6635.

(29) Fischer, P. J.; Do, M. P.; Reich, R. M.; Nagasubramanian, A.; Srinivasan, M.; Kühn, F. E. Synthesis and Physicochemical Characterization of Room Temperature Ionic Liquids and Their Application in Sodium Ion Batteries. *Phys. Chem. Chem. Phys.* **2018**, *20* (46), 29412−29422.

(30) Monti, D.; Jónsson, E.; Palacín, M. R.; Johansson, P. Ionic Liquid Based Electrolytes for Sodium-Ion Batteries: Na+ Solvation and Ionic Conductivity. *J. Power Sources* **2014**, *245*, 630−636.

(31) Anderson, E. B.; Long, T. E. Imidazole- and Imidazolium-Containing Polymers for Biology and Material Science Applications. *Polymer* **2010**, *51*, 2447−2454.

(32) Li, Q.; Wang, S.; Zhou, M.; Lu, X.; Qiao, G.; Li, C.; Wu, Y. A Review of Imidazolium Ionic Liquid-Based Phase Change Materials for Low and Medium Temperatures Thermal Energy Storage and Their Applications. *GER* **2023**, *1*, 100010.

(33) MacFarlane, D. R.; Meakin, P.; Sun, J.; Amini, N.; Forsyth, M. Pyrrolidinium Imides: A New Family of Molten Salts and Conductive Plastic Crystal Phases. *J. Phys. Chem. B* **1999**, *103* (20), 4164−4170.

(34) Forsyth, C. M.; MacFarlane, D. R.; Golding, J. J.; Huang, J.; Sun, J.; Forsyth, M. Structural Characterization of Novel Ionic Materials Incorporating the Bis(Trifluoromethanesulfonyl)Amide Anion. *Chem. Mater.* **2002**, *14* (5), 2103−2108.

(35) Bazito, F. F. C.; Silveira, L. T.; Torresi, R. M.; Córdoba de Torresi, S. I. Spectroelectrochemical Study of a Soluble Derivative of Poly(Aniline) in a Room Temperature Ionic Liquid. *Electrochim. Acta* **2007**, *53* (3), 1217−1224.

(36) Monteiro, M. J.; Bazito, F. F. C.; Siqueira, L. J. A.; Ribeiro, M. C. C.; Torresi, R. M. Transport Coefficients, Raman Spectroscopy, and Computer Simulation of Lithium Salt Solutions in an Ionic Liquid. *J. Phys. Chem. B* **2008**, *112* (7), 2102−2109.

https://doi.org/10.1021/acs.jpcb.5c07871
J. Phys. Chem. B XXXX, XXX, XXX−XXX

(37) Liu, G.; Wen, L.; Li, Y.; Kou, Y. Synthesis and Electrochemical Properties of P2-Na2/3Ni1/3Mn2/3O2. *Ionics* **2015**, *21* (4), 1011−1016.
(38) Wang, P. F.; You, Y.; Yin, Y. X.; Wang, Y. S.; Wan, L. J.; Gu, L.; Guo, Y. G. Suppressing the P2−O2 Phase Transition of Na0.67Mn0.67Ni0.33O2by Magnesium Substitution for Improved Sodium-Ion Batteries. *Angew. Chem., Int. Ed.* **2016**, *55* (26), 7445−7449.
(39) Zhu, H.; Yao, Z.; Zhu, H.; Huang, Y.; Zhang, J.; Li, C. C.; Wiaderek, K. M.; Ren, Y.; Sun, C. J.; Zhou, H.; Fan, L.; Chen, Y.; Xia, H.; Gu, L.; Lan, S.; Liu, Q. Unblocking Oxygen Charge Compensation for Stabilized High-Voltage Structure in P2-Type Sodium-Ion Cathode. *Advanced Science* **2022**, *9* (16), 2200498.
(40) Xiao, J.; Li, Q.; Bi, Y.; Cai, M.; Dunn, B.; Glossmann, T.; Liu, J.; Osaka, T.; Sugiura, R.; Wu, B.; Yang, J.; Zhang, J. G.; Whittingham, M. S. Understanding and Applying Coulombic Efficiency in Lithium Metal Batteries. *Nat. Energy* **2020**, *5* (8), 561−568.
(41) Adams, B. D.; Zheng, J.; Ren, X.; Xu, W.; Zhang, J. G. Accurate Determination of Coulombic Efficiency for Lithium Metal Anodes and Lithium Metal Batteries. *Adv. Energy Mater.* **2018**, *8* (7), 1702097.
(42) Leite, M. M.; Martins, V. L.; Vichi, F. M.; Torresi, R. M. Electrochemistry of Sodium Titanate Nanotubes as a Negative Electrode for Sodium-Ion Batteries. *Electrochim. Acta* **2020**, *331*, 135422.
(43) Chauque, S.; Braga, A. H.; Gonçalves, R. V.; Rossi, L. M.; Torresi, R. M. Enhanced Energy Storage of Fe3O4 Nanoparticles Embedded in N-Doped Graphene. *ChemElectroChem.* **2020**, *7* (6), 1456−1464.
(44) Ong, S. P.; Chevrier, V. L.; Hautier, G.; Jain, A.; Moore, C.; Kim, S.; Ma, X.; Ceder, G. Voltage, Stability and Diffusion Barrier Differences between Sodium-Ion and Lithium-Ion Intercalation Materials. *Energy Environ. Sci.* **2011**, *4* (9), 3680−3688.
(45) Sanchez-Ramirez, N.; Martins, V. L.; Ando, R. A.; Camilo, F. F.; Urahata, S. M.; Ribeiro, M. C. C.; Torresi, R. M. Physicochemical Properties of Three Ionic Liquids Containing a Tetracyanoborate Anion and Their Lithium Salt Mixtures. *J. Phys. Chem. B* **2014**, *118* (29), 8772−8781.
(46) Moreno, M.; Simonetti, E.; Appetecchi, G. B.; Carewska, M.; Montanino, M.; Kim, G.-T.; Loeffler, N.; Passerini, S. Ionic Liquid Electrolytes for Safer Lithium Batteries. *J. Electrochem. Soc.* **2017**, *164* (1), A6026−A6031.
(47) Tong, J.; Wu, S.; von Solms, N.; Liang, X.; Huo, F.; Zhou, Q.; He, H.; Zhang, S. The Effect of Concentration of Lithium Salt on the Structural and Transport Properties of Ionic Liquid-Based Electrolytes. *Front Chem.* **2020**, *7*, 945.
(48) Valderrama, J. O.; Campusano, R. A.; Rojas, R. E. Glass Transition Temperature of Ionic Liquids Using Molecular Descriptors and Artificial Neural Networks. *C. R. Chim.* **2017**, *20* (5), 573−584.
(49) Sánchez-Ramírez, N.; Assresahegn, B. D.; Bélanger, D.; Torresi, R. M. A Comparison among Viscosity, Density, Conductivity, and Electrochemical Windows of N-n-Butyl-N-Methylpyrrolidinium and Triethyl-n-Pentylphosphonium Bis(Fluorosulfonyl Imide) Ionic Liquids and Their Analogues Containing Bis-(Trifluoromethylsulfonyl) Imide Anion. *J. Chem. Eng. Data* **2017**, *62* (10), 3437−3444.
(50) Martins, V. L.; Sanchez-Ramirez, N.; Ribeiro, M. C. C.; Torresi, R. M. Two Phosphonium Ionic Liquids with High Li+ Transport Number. *Phys. Chem. Chem. Phys.* **2015**, *17* (35), 23041−23051.
(51) Ahmed, M.; Bhowmick, S.; Filippov, A.; Johansson, P.; Shah, F. U. Ionic Liquids and Electrolytes with Flexible Aromatic Anions. *Chem.—Eur. J.* **2023**, *29*, No. e202301000.
(52) Palumbo, O.; Paolone, A.; Philippi, F.; Rauber, D.; Welton, T. Dynamics in Quaternary Ionic Liquids with Non-Flexible Anions: Insights from Mechanical Spectroscopy. *Int. J. Mol. Sci.* **2023**, *24* (13), 11046.
(53) González, B.; González, E. J. Physical Properties of the Pure 1-Methyl-1-Propylpyrrolidinium Bis(Trifluoromethylsulfonyl)Imide Ionic Liquid and Its Binary Mixtures with Alcohols. *J. Chem. Thermodyn.* **2014**, *68*, 109−116.
(54) Rauber, D.; Hofmann, A.; Philippi, F.; Kay, C. W. M.; Zinkevich, T.; Hanemann, T.; Hempelmann, R. Structure-Property Relation of Trimethyl Ammonium Ionic Liquids for Battery Applications. *Appl. Sci.* **2021**, *11* (12), 5679.
(55) Harris, K. R.; Kanakubo, M. Self-Diffusion Coefficients and Related Transport Properties for a Number of Fragile Ionic Liquids. *J. Chem. Eng. Data* **2016**, *61* (7), 2399−2411.
(56) Xu, H.; Zhang, D. Viscosities and Conductivities of [BMIM]Zn(Ac)XCly(X = 0,1,2,3; Y = 3,2,1,0) Ionic Liquids at Different Temperatures. *J. Chem.* **2017**, *2017* (1), 7428097.
(57) Ikeda, M.; Aniya, M. Understanding the Vogel-Fulcher-Tammann Law in Terms of the Bond Strength-Coordination Number Fluctuation Model. *J. Non Cryst. Solids* **2013**, *371*−*372*, 53−57.
(58) Sánchez-Ramírez, N.; Monje, I. E.; Martins, V. L.; Bélanger, D.; Camargo, P. H. C.; Torresi, R. M. Four Phosphonium-Based Ionic Liquids. Synthesis, Characterization and Electrochemical Performance as Electrolytes for Silicon Anodes. *ChemistrySelect* **2022**, *7* (4), No. e202104430.
(59) Paduszyński, K.; Domańska, U. Viscosity of Ionic Liquids: An Extensive Database and a New Group Contribution Model Based on a Feed-Forward Artificial Neural Network. *J. Chem. Inf. Model.* **2014**, *54* (5), 1311−1324.
(60) ZhouMatsumoto, Z. B. H.; Tatsumi, K.; Tatsumi, K. Cyclic Quaternary Ammonium Ionic Liquids with Perfluoroalkyltrifluoroborates: Synthesis, Characterization, and Properties. *Chem.—Eur. J.* **2006**, *12* (8), 2196−2212.
(61) Appetecchi, G. B.; Montanino, M.; Carewska, M.; Moreno, M.; Alessandrini, F.; Passerini, S. Chemical-Physical Properties of Bis(Perfluoroalkylsulfonyl)Imide-Based Ionic Liquids. *Electrochim. Acta* **2011**, *56* (3), 1300−1307.
(62) Tsunashima, K.; Sugiya, M. Physical and Electrochemical Properties of Low-Viscosity Phosphonium Ionic Liquids as Potential Electrolytes. *Electrochem commun* **2007**, *9* (9), 2353−2358.
(63) Nancarrow, P.; Al-Othman, A.; Mital, D. K.; Döpking, S. Comprehensive Analysis and Correlation of Ionic Liquid Conductivity Data for Energy Applications. *Energy* **2021**, *220*, 119761.
(64) Sanchez-Ramirez, N.; Assresahegn, B. D.; Torresi, R. M.; Bélanger, D. Producing High-Performing Silicon Anodes by Tailoring Ionic Liquids as Electrolytes. *Energy Storage Mater.* **2020**, *25* (February 2019), 477−486.
(65) Hu, P.; Jiang, W.; Zhong, L.; Zhou, S. Physicochemical Properties of Amide−AlCl3 Based Ionic Liquid Analogues and Their Mixtures with Copper Salt. *Chin. J. Chem. Eng.* **2019**, *27* (1), 144−149.
(66) Asenbauer, J.; Ben Hassen, N.; McCloskey, B. D.; Prausnitz, J. M. Solubilities and Ionic Conductivities of Ionic Liquids Containing Lithium Salts. *Electrochim. Acta* **2017**, *247*, 1038−1043.
(67) Hakim, L.; Ishii, Y.; Matsumoto, K.; Hagiwara, R.; Ohara, K.; Umebayashi, Y.; Matubayasi, N. Transport Properties of Ionic Liquid and Sodium Salt Mixtures for Sodium-Ion Battery Electrolytes from Molecular Dynamics Simulation with a Self-Consistent Atomic Charge Determination. *J. Phys. Chem. B* **2020**, *124* (33), 7291−7305.
(68) Noor, S. A. M.; Su, N. C.; Khoon, L. T.; Mohamed, N. S.; Ahmad, A.; Yahya, M. Z. A.; Zhu, H.; Forsyth, M.; MacFarlane, D. R. Properties of High Na-Ion Content N-Propyl-N-Methylpyrrolidinium Bis(Fluorosulfonyl)Imide -Ethylene Carbonate Electrolytes. *Electrochim. Acta* **2017**, *247*, 983−993.
(69) Chaban, V. V.; Andreeva, N. A. Sodium-Ion Electrolytes Based on Ionic Liquids: A Role of Cation-Anion Hydrogen Bonding. *J. Mol. Model* **2016**, *22* (8), 172.
(70) Brutti, S.; Navarra, M. A.; Maresca, G.; Panero, S.; Manzi, J.; Simonetti, E.; Appetecchi, G. B. Ionic Liquid Electrolytes for Room Temperature Sodium Battery Systems. *Electrochim. Acta* **2019**, *306*, 317−326.
(71) Massaro, A.; Avila, J.; Goloviznina, K.; Rivalta, I.; Gerbaldi, C.; Pavone, M.; Costa Gomes, M. F.; Padua, A. A. H. Sodium Diffusion in Ionic Liquid-Based Electrolytes for Na-Ion Batteries: The Effect of

https://doi.org/10.1021/acs.jpcb.5c07871
J. Phys. Chem. B XXXX, XXX, XXX−XXX

Polarizable Force Fields. *Phys. Chem. Chem. Phys.* **2020**, *22* (35), 20114−20122.
(72) Velho, P.; Lopes, C.; Macedo, E. A. Predicting the Ionicity of Ionic Liquids in Binary Mixtures Based on Solubility Data: II. *Fluid Phase Equilib.* **2023**, *569*, 113766.
(73) MacFarlane, D. R.; Forsyth, M.; Izgorodina, E. I.; Abbott, A. P.; Annat, G.; Fraser, K. On the Concept of Ionicity in Ionic Liquids. *Phys. Chem. Chem. Phys.* **2009**, *11* (25), 4962−4967.
(74) Moganty, S. S.; Srivastava, S.; Lu, Y.; Schaefer, J. L.; Rizvi, S. A.; Archer, L. A. Ionic Liquid-Tethered Nanoparticle Suspensions: A Novel Class of Ionogels. *Chem. Mater.* **2012**, *24* (7), 1386−1392.
(75) Safna Hussan, K. P.; Thayyil, M. S. Charge Transport and Glassy Dynamics in a Room Temperature Ionic Liquid- [BMPyr]-[TFSI]. *J. Non Cryst. Solids* **2020**, *541*, 120133.
(76) Musiał, M.; Wojnarowska, Z.; Cheng, S.; Ngai, K. L.; Paluch, M. Evidence of a Fundamental Mechanism Governing Conductivity Relaxation in Room-Temperature Ionic Liquid. *J. Phys. Chem. C* **2019**, *123* (36), 22089−22094.
(77) Stigliano, P.; Ferrara, C.; Pianta, N.; Gentile, A.; Mezzomo, L.; Lorenzi, R.; Berbenni, V.; Ruffo, R.; Appetecchi, G. B.; Mustarelli, P. Physicochemical Properties of Pyr13TFSI-NaTFSI Electrolyte for Sodium Batteries. *Electrochim. Acta* **2022**, *412*, 140123.
(78) Chagas, L. G.; Jeong, S.; Hasa, I.; Passerini, S. Ionic Liquid-Based Electrolytes for Sodium-Ion Batteries: Tuning Properties to Enhance the Electrochemical Performance of Manganese-Based Layered Oxide Cathode. *ACS Appl. Mater. Interfaces* **2019**, *11* (25), 22278−22289.
(79) Zilinskaite, S.; Rennie, A. J. R.; Boston, R.; Reeves-Mclaren, N. Biotemplating: A Sustainable Synthetic Methodology for Na-Ion Battery Materials. *J. Mater. Chem. A Mater.* **2018**, *6* (13), 5346−5355.
(80) Wang, K.; Yan, P.; Sui, M. Phase Transition Induced Cracking Plaguing Layered Cathode for Sodium-Ion Battery. *Nano Energy* **2018**, *54* (September), 148−155.
(81) Dang, R.; Chen, M.; Li, Q.; Wu, K.; Lee, Y. L.; Hu, Z.; Xiao, X. Na + -Conductive Na 2 Ti 3 O 7 -Modified P2-Type Na 2/3 Ni 1/3 Mn 2/3 O 2 via a Smart in Situ Coating Approach: Suppressing Na +/Vacancy Ordering and P2-O2 Phase Transition. *ACS Appl. Mater. Interfaces* **2019**, *11* (1), 856−864.
(82) Wang, X.; Yin, X.; Feng, X.; Li, Y.; Dong, X.; Shi, Q.; Zhao, Y.; Zhang, J. Rational Design of Na0.67Ni0.2Co0.2Mn0.6O2Micro-sphere Cathode Material for Stable and Low Temperature Sodium Ion Storage. *Chem. Eng. J.* **2022**, *428*, 130990.
(83) Lu, Z.; Dahn, J. R. In Situ X-Ray Diffraction Study of P2-Na[Sub 2/3][Ni[Sub 1/3]Mn[Sub 2/3]]O[Sub 2]. *J. Electrochem. Soc.* **2001**, *148* (11), A1225.
(84) Wen, Y.; Wang, B.; Zeng, G.; Nogita, K.; Ye, D.; Wang, L. Electrochemical and Structural Study of Layered P2-Type Na2/3Ni1/3Mn2/3O2 as Cathode Material for Sodium-Ion Battery. *Chem.−Asian J.* **2015**, *10* (3), 661−666.
(85) Wang, H.; Yang, B.; Liao, X. Z.; Xu, J.; Yang, D.; He, Y. S.; Ma, Z. F. Electrochemical Properties of P2-Na2/3[Ni1/3Mn 2/3]O2 Cathode Material for Sodium Ion Batteries When Cycled in Different Voltage Ranges. *Electrochim. Acta* **2013**, *113*, 200−204.
(86) Liu, Q.; Hu, Z.; Chen, M.; Zou, C.; Jin, H.; Wang, S.; Gu, Q.; Chou, S. P2-Type Na2/3Ni1/3Mn2/3O2 as a Cathode Material with High-Rate and Long-Life for Sodium Ion Storage. *J. Mater. Chem. A Mater.* **2019**, *7* (15), 9215−9221.
(87) Liu, Y.; Wang, C.; Zhao, S.; Zhang, L.; Zhang, K.; Li, F.; Chen, J. Mitigation of Jahn-Teller Distortion and Na+/Vacancy Ordering in a Distorted Manganese Oxide Cathode Material by Li Substitution. *Chem. Sci.* **2021**, *12* (3), 1062−1067.
(88) Park, M. S.; Veerasubramani, G. K.; Thangavel, R.; Lee, Y. S.; Kim, D. W. Effect of Organic Solvents on the Electrochemical Performance of Sodium-Ion Hybrid Capacitors. *ChemElectroChem.* **2019**, *6* (3), 653−660.
(89) Ponrouch, A.; Marchante, E.; Courty, M.; Tarascon, J. M.; Palacín, M. R. In Search of an Optimized Electrolyte for Na-Ion Batteries. *Energy Environ. Sci.* **2012**, *5* (9), 8572−8583.
(90) Kurzweil, P.; Scheuerpflug, W.; Frenzel, B.; Schell, C.; Schottenbauer, J. Differential Capacity as a Tool for SOC and SOH Estimation of Lithium Ion Batteries Using Charge/Discharge Curves, Cyclic Voltammetry, Impedance Spectroscopy, and Heat Events: A Tutorial. *Energies (Basel)* **2022**, *15* (13), 4520.
(91) Spitthoff, L.; Vie, P. J. S.; Wahl, M. S.; Wind, J.; Burheim, O. S. Incremental Capacity Analysis (DQ/DV) as a Tool for Analysing the Effect of Ambient Temperature and Mechanical Clamping on Degradation. *J. Electroanal. Chem.* **2023**, *944*, 117627.
(92) Buchholz, D.; Chagas, L. G.; Winter, M.; Passerini, S. P2-Type Layered Na0.45Ni0.22Co0.11Mn 0.66O2 as Intercalation Host Material for Lithium and Sodium Batteries. *Electrochim. Acta* **2013**, *110*, 208−213.
(93) He, H.; Sun, D.; Tang, Y.; Wang, H.; Shao, M. Understanding and Improving the Initial Coulombic Efficiency of High-Capacity Anode Materials for Practical Sodium Ion Batteries. *Energy Storage Mater.* **2019**, *23*, 233−251.
(94) Mohammadi, A.; Djafer, S.; Sayegh, S.; Naylor, A. J.; Bechelany, M.; Younesi, R.; Monconduit, L.; Stievano, L. Assessing Coulombic Efficiency in Lithium Metal Anodes. *Chem. Mater.* **2023**, *35* (6), 2381−2393.
(95) Madani, S. S.; Schaltz, E.; Knudsen Kær, S. Effect of Current Rate and Prior Cycling on the Coulombic Efficiency of a Lithium-Ion Battery. *Batteries* **2019**, *5* (3), 57.
(96) Wang, S.; Fan, Y.; Stroe, D.-I.; Fernandez, C.; Yu, C.; Cao, W.; Chen, Z. Lithium-Ion Battery Characteristics and Applications. In *Battery System Modeling*; Elsevier, 2021; pp 1−46.
(97) Ariyoshi, K.; Siroma, Z.; Mineshige, A.; Takeno, M.; Fukutsuka, T.; Abe, T.; Uchida, S. Electrochemical Impedance Spectroscopy Part 1: Fundamentals. *Electrochemistry* **2022**, *90* (10), 102007.
(98) Lazanas, A. C.; Prodromidis, M. I. Electrochemical Impedance Spectroscopy−A Tutorial. *ACS Meas. Sci. Au* **2023**, *3*, 162−193.
(99) Winter, R. F. Half-Wave Potential Splittings ΔE1/2 as a Measure of Electronic Coupling in Mixed-Valent Systems: Triumphs and Defeats. *Organometallics* **2014**, *33* (18), 4517−4536.
(100) Pospisil, J.; Marackova, L.; Zmeskal, O.; Kovalenko, A. Universal Approach for Diffusion Quantification Applied to Lead Halide Perovskite Single Crystals. *Appl. Phys. A Mater. Sci. Process* **2023**, *129* (2), 129.
(101) Gharbi, O.; Tran, M. T. T.; Tribollet, B.; Turmine, M.; Vivier, V. Revisiting Cyclic Voltammetry and Electrochemical Impedance Spectroscopy Analysis for Capacitance Measurements. *Electrochim. Acta* **2020**, *343*, 136109.
(102) Orazem, M. E. Measurement Model for Analysis of Electrochemical Impedance Data. *J. Solid State Electrochem.* **2024**, *28* (3−4), 1273−1289.
(103) Leifer, N.; Aurbach, D.; Greenbaum, S. G. NMR Studies of Lithium and Sodium Battery Electrolytes. *Prog. Nucl. Magn. Reson. Spectrosc.* **2024**, *142*−*143*, 1−54.
(104) Morales, D.; Chagas, L. G.; Paterno, D.; Greenbaum, S.; Passerini, S.; Suarez, S. Transport Studies of NaPF6 Carbonate Solvents-Based Sodium Ion Electrolytes. *Electrochim. Acta* **2021**, *377*, 138062.
(105) Karatrantos, A. V.; Middendorf, M.; Nosov, D. R.; Cai, Q.; Westermann, S.; Hoffmann, K.; Nurnberg, P.; Shaplov, A. S.; Schonhoff, M. Diffusion and Structure of Propylene Carbonate-Metal Salt Electrolyte Solutions for Post-Lithium-Ion Batteries: From Experiment to Simulation. *J. Chem. Phys.* **2024**, *161* (5), 054502.
(106) Richardson, P. M.; Voice, A. M.; Ward, I. M. Pulsed-Field Gradient NMR Self Diffusion and Ionic Conductivity Measurements for Liquid Electrolytes Containing Libf4 and Propylene Carbonate. *Electrochim. Acta* **2014**, *130*, 606−618.
(107) Friedman, R. Density Functional Theory Calculations Unravel the Structure and Dynamics of NaClO4 and NaPF6 Salts in Sodium-Ion Batteries. *J. Phys. Chem. C* **2025**, *129* (3), 1575−1581.
(108) Sakti, A. W.; Wahyudi, S. T.; Ahmad, F.; Darmawan, N.; Hardhienata, H.; Alatas, H. Effects of Salt Concentration on the Water and Ion Self-Diffusion Coefficients of a Model Aqueous

https://doi.org/10.1021/acs.jpcb.5c07871
J. Phys. Chem. B XXXX, XXX, XXX−XXX

Sodium-Ion Battery Electrolyte. *J. Phys. Chem. B* **2022**, *126* (11), 2256−2264.
(109) Kubisiak, P.; Wróbel, P.; Eilmes, A. How Temperature, Pressure, and Salt Concentration Affect Correlations in LiTFSI/EMIM-TFSI Electrolytes: A Molecular Dynamics Study. *J. Phys. Chem. B* **2021**, *125* (44), 12292−12302.
(110) Forsyth, M.; Yoon, H.; Chen, F.; Zhu, H.; MacFarlane, D. R.; Armand, M.; Howlett, P. C. Novel Na+ Ion Diffusion Mechanism in Mixed Organic-Inorganic Ionic Liquid Electrolyte Leading to High Na+ Transference Number and Stable, High Rate Electrochemical Cycling of Sodium Cells. *J. Phys. Chem. C* **2016**, *120* (8), 4276−4286.
(111) Bouguern, M. D.; M R, A. K.; Zaghib, K. The Critical Role of Interfaces in Advanced Li-Ion Battery Technology: A Comprehensive Review. *J. Power Sources* **2024**, *623*, 235457.
(112) Wang, H.; Li, X.; Li, F.; Liu, X.; Yang, S.; Ma, J. Formation and Modification of Cathode Electrolyte Interphase: A Mini Review. *Electrochem. Commun.* **2021**, *122*, 106870.
(113) Nobili, F.; Croce, F.; Scrosati, B.; Marassi, R. Electronic and Electrochemical Properties of LixNi1-YCoyO2 Cathodes Studied by Impedance Spectroscopy. *Chem. Mater.* **2001**, *13* (5), 1642−1646.
(114) Carboni, M.; Manzi, J.; Armstrong, A. R.; Billaud, J.; Brutti, S.; Younesi, R. Analysis of the Solid Electrolyte Interphase on Hard Carbon Electrodes in Sodium-Ion Batteries. *ChemElectroChem.* **2019**, *6* (6), 1745−1753.
(115) Linsenmann, F.; Pritzl, D.; Gasteiger, H. A. A Reference Electrode for In Situ Impedance Measurements in Sodium-Ion Batteries. *J. Electrochem. Soc.* **2019**, *166* (15), A3668−A3674.
(116) Jang, J. Y.; Kim, H.; Lee, Y.; Lee, K. T.; Kang, K.; Choi, N. S. Cyclic Carbonate Based-Electrolytes Enhancing the Electrochemical Performance of Na4Fe3(PO4)2(P 2O7) Cathodes for Sodium-Ion Batteries. *Electrochem commun* **2014**, *44*, 74−77.
(117) Huang, J. Diffusion Impedance of Electroactive Materials, Electrolytic Solutions and Porous Electrodes: Warburg Impedance and Beyond. *Electrochim. Acta* **2018**, *281*, 170−188.
(118) Choi, W.; Shin, H. C.; Kim, J. M.; Choi, J. Y.; Yoon, W. S. Modeling and Applications of Electrochemical Impedance Spectroscopy (Eis) for Lithium-Ion Batteries. *J. Electrochem. Sci. Technol.* **2020**, *11*, 1−13.
(119) Do, M. P.; Bucher, N.; Nagasubramanian, A.; Markovits, I.; Bingbing, T.; Fischer, P. J.; Loh, K. P.; Kühn, F. E.; Srinivasan, M. Effect of Conducting Salts in Ionic Liquid Electrolytes for Enhanced Cyclability of Sodium-Ion Batteries. *ACS Appl. Mater. Interfaces* **2019**, *11* (27), 23972−23981.
(120) Kotronia, A.; Asfaw, H. D.; Tai, C. W.; Hahlin, M.; Brandell, D.; Edström, K. Nature of the Cathode-Electrolyte Interface in Highly Concentrated Electrolytes Used in Graphite Dual-Ion Batteries. *ACS Appl. Mater. Interfaces* **2021**, *13* (3), 3867−3880.

https://doi.org/10.1021/acs.jpcb.5c07871
J. Phys. Chem. B XXXX, XXX, XXX−XXX